

Microwave structures for generating stable arrays of microplasmas

A thesis
Submitted by

Chen Wu

In partial fulfillment of the requirements
for the degree of

Master of Science

In

Electrical Engineering

TUFTS UNIVERSITY

May 2011

Copyright (2011) by Chen Wu

Advisor: Prof. Jeffrey A. Hopwood

Abstract:

Various microwave circuit structures are investigated and shown to support extended arrays of cold microplasmas. Non-thermal or cold microplasma has been intensively investigated because the gas temperature remains low, even at atmospheric pressure. This suggests that atmospheric pressure plasmas may replace arcs and plasma torches in temperature-sensitive applications including treatment of polymers and biomaterials. This thesis builds on the concept that quarter-wave resonators, in the form of microstrip transmission lines, can sustain cold microplasmas. While small linear arrays of such resonators were previously shown to sustain up to 24 microplasmas, the intrinsically weak coupling between resonators was found to be insufficient for longer, more uniform arrays. An electrical connection between each resonator (called a coupling strip) is shown to enhance the coupling among resonators, allowing arrays composed of at least 72 elements that extend 90 mm in length. In addition to linear microplasma arrays, circular-shaped microplasmas have also been demonstrated. Theoretical development of an electromagnetic coupling model known as coupled mode theory shows good agreement with experimental measurements of microplasma emission intensity as well as electromagnetic simulations of these devices. Prospects for scaling the microplasma array to greater lengths are described. These findings may allow for future low-cost plasma processing using roll-to-roll techniques at pressures of one atmosphere.

Acknowledgements:

First and foremost, I would like to express my deep and sincere gratitude to my academic and thesis advisor, Professor Jeffrey A. Hopwood who introduced me to this wonderland of plasma physics and engineering. During the past two years, he has been a patient and knowledgeable tutor. I appreciate his academic advice, guidance, and supervision. I am inspired by his comprehensive thinking and foresight, and I enjoy having discussion with him. Special thanks for his comments during the preparation of this thesis.

I wish to thank Professor Panzer and Professor Hoskinson on my committee for their interest and time spent reviewing my thesis.

I would like to acknowledge the support and help of Prof. Hoskinson and colleague Naoto Miura. They have enriched my knowledge of plasma engineering. With Prof. Hoskinson's help, I learned about iCCD camera and spectrometer operation. I am enjoying my stay at Sci-Tech and all the delightful conversations.

I am grateful to my parents for their love and encouragement. They have provided much support to me during my graduate study.

Finally, I would like to acknowledge generous funding from the United States Department of Energy under award No. DE-SC0001923.

Table of Contents

1. Introduction.....	1
1.1 Single microplasma sources	1
1.1.1 Plasma background information.....	1
1.1.2 DBD plasma source	1
1.1.3 Plasma jets.....	2
1.1.4 Other plasma sources	3
1.2 Plasma arrays	3
1.3 Circular and linear arrays basic structure	5
1.3.1 Circular array	6
1.3.2 Linear array	7
1.4 Research Objective.....	8
1.4.1 Scientific understanding	8
1.4.2 Application perspective	8
2. Theory	9
2.1 Quarter-wave resonator model	9
2.2 Coupled mode theory introduction	12
2.2.1 CMT differential equation matrix interpretation	13
2.2.2 Generic CMT linear equation set for 5 resonators	13
2.2.3 Linear array CMT matrix representation	14
2.2.4 Linear array equation set solution	15
2.2.5 Linear equation set solution with direct coupling method	17
2.2.6 Circular array CMT matrix representation	18
2.2.7 Circular array equation set solution	19
2.2.8 CMT estimate of plasma effect on the circular array	20
2.2.9 Higher modes of circular and linear arrays	22
2.3 Theoretical magnetic and electric coupling mechanisms and coupling coefficient modeling	24
3. Simulation Results	29
3.1 Circular array	29

3.1.1	S-parameter of the circular array	29
3.1.2	E-field and higher modes discussion for the circular array	30
3.2	Linear array	31
3.2.1	E-field and S-parameter without DSC	32
3.2.2	E-field with DSC	33
3.2.3	E-field and current patterns of higher modes	35
3.3	Magnetic and electric coupling demonstration	38
4.	Experimental Results	41
4.1	Experimental setup and procedure.....	41
4.2	Circular array.....	42
4.2.1	Side port 1 st and 4 th modes.....	42
4.2.2	Improving uniformity with dielectric limiters.....	43
4.3	Linear array.....	45
4.3.1	First mode uniform plasma with dielectric limiters.....	45
4.3.2	Higher modes in comparison with simulations	49
5.	Conclusion and Future work	50
5.1	Uniform plasma arrays with RF sources at atmospheric pressure	50
5.2	Future work	50
5.2.1	Higher frequency operation	50
5.2.2	Increase power level to support large number of resonators	51
5.2.3	Instability study	51
6.	References	52
Appendices		
Appendix A: MATLAB code for CMT model of 72-resonator linear array.....		56
Appendix B: MATLAB code for CMT model of 72-resonator array with DCS...		58
Appendix C: MATLAB code for CMT model of circular array without plasma effect		60
Appendix D: MATLAB code for CMT model of circular array with plasma effect		61

List of Figures

Figure 1.1 Common dielectric barrier discharge electrode configurations. [After Ref 1]	(2)
Figure 1.2 Schematic of a typical plasma jet. [After Ref 3].....	(2)
Figure 1.3 Two dimensional 10*10(50 μ m diameter) DC microplasma array in helium at 1000Torr [After Ref. 17]	(4)
Figure 1.4 Image of a seven-channel honeycomb spatially extended atmospheric (SEAP) DBD plasma jet array in helium flow (a) and a 31-jet SEAP array in helium flow (b) [After Ref. 18]	(5)
Figure 1.5 Photograph of circular plasma array circuit composed of six resonators. Power is delivered to the bottom resonator (denoted as 1) through SMA connector	(6)
Figure 1.6 Photograph of 72-resonator linear plasma array circuit of new design with direct coupling strip. Plasma is generated in the gap with total length of 90mm. Power is transferred to the under-port input connector on the back side	(7)
Figure 2.1 Photograph of a microstrip split-ring resonator (MSRR) plasma source with quarter-wavelength matching. [After Ref 19]	(10)
Figure 2.2 Circuit model of the input impedance of a lossy transmission line of length l , characteristic impedance Z_0 and wave number β , loaded with Z_L	(10)
Figure 2.3 (a) Photograph of quarter-wavelength resonator with a piece of ground plane closed placed to the open-circuited end	(12)
(b) Equivalent circuit of the resonator and voltage magnitude plotted along the length. [After Ref 22]	(12)
Figure 2.4 Relative power distribution in mode 1(O) of the 72-resonator linear plasma array according to CMT without the direct coupling strip effect	(17)
Figure 2.5 Relative power distributed on each resonator of the circular plasma array for different modes according to CMT [Ref 24]	(20)

Figure 2.6 Resonant frequency shifting due to the presence of plasma impedance

$$Z_p = R_p + jX_p = 495 - j910 \text{ for a single resonator} \dots\dots\dots(21)$$

Figure 2.7 Power distribution of mode 1 and 4 when the resonant frequency of the first resonator is shifted down by 20MHz with the other five remaining unaltered [After Ref 24] \dots\dots\dots(22)

Figure 2.8 Relative power distribution in 2nd mode (—) and 3rd mode (----) of linear plasma array in normalized magnitude according to CMT without direct coupling strip effect \dots\dots\dots (24)

Figure 2.9 The lumped circuit model of electrical coupling (on the left) and magnetic coupling (on the right) of two closely placed resonators. [After Ref 33] \dots\dots\dots(26)

Figure 3.1 Simulation result and experimental measurement of the reflection coefficient of the circular array without plasma \dots\dots\dots (30)

Figure 3.2 Illustration of simulation results in gray scale of the electric field strength of the circular plasma array in the 1st mode (a) and 4th mode (b) \dots\dots\dots (30)

Figure 3.3 Illustration of simulation result in gray scale of the electric field strength along the gap of 36-resonator linear array without direct coupling strip in the 1st mode \dots\dots\dots(32)

Figure 3.4 Illustration of simulation result in gray scale of the electric field strength along the gap of 36-resonator linear array with direct coupling strip in the 1st mode \dots\dots\dots (33)

Figure 3.5 Simulation results of electric field along the gap of 36-resonator linear plasma arrays with and without direct coupling strip \dots\dots\dots (34)

Figure 3.6 HFSS simulation result of S-parameter in magnitude of a 72-resonator array with direct coupling strip \dots\dots\dots(36)

Figure 3.7 Simulation electric field results of a 72-resonator array with direct coupling strip in mode 3 and mode 5 \dots\dots\dots (37)

Figure 3.8 Simulation result of surface current at 1st , 3rd and 5th mode of 72-resonator array \dots\dots\dots(38)

Figure 3.9 Simulation results of surface current density on two coupled microstrip quarter-wave resonators at even mode (a) and odd mode (b) \dots\dots\dots(39)

Figure 3.10 Simulation results of electric field at tips of two coupled microstrip quarter-wave resonators at even mode (a) and odd mode (b)	(40)
Figure 3.11 Simulation results of magnetic field in the substrate at vias of two coupled microstrip quarter-wave resonators at even mode (a) and odd mode (b)	(40)
Figure 4.1 Photo of a circular argon plasma array in the 1 st mode at 720Torr with input power of 1.8W	(42)
Figure 4.2 Photo of a circular argon plasma array in the 4 th mode at 720Torr with input power of 2.0W.....	(43)
Figure 4.3 Photograph of a circular argon plasma array operating at 1 st mode (0.99GHz, 1atm 2.5W) with plasma dielectric limiter added to the array. Inset: photo of the same plasma taken without photoflash light.....	(44)
Figure 4.4 Relative plasma emission intensity near each resonator of the circular array (full scale=255).....	(45)
Figure 4.5 Linear argon plasma array in mode 1 without direct coupling strip generated at 500Torr with input power of 26 Watts.....	(46)
Figure 4.6 Linear argon plasma array in mode 1 with direct coupling strip generated at 750Torr with input power of 18 Watts.	(47)
Figure 4.7 Photograph of experimental 72-element linear plasma array in argon at 750Torr (1 atm) with input power of 20.9 Watts in the 1 st mode.....	(48)
Figure 4.8 Emission intensity of the 90mm linear argon plasma array with dielectric limiters as shown in the lower part of figure 4.7.....	(48)
Figure 4.9 Photo of experimental argon plasma in 3 rd and 5 th mode at 750Torr (1atm) with dielectric cap limiters.....	(49)

Microwave structures for generating stable arrays of microplasmas

1. Introduction

1.1 Single microplasma sources

1.1.1 Plasma background info

Plasma, known as the fourth state of matter, is typically composed of gases, electrons and ionized particles. Plasma can be categorized as thermal and non-thermal plasma for different conditions. Electrons are usually much more energetic than both ions and neutral gas particles due to their small mass. Plasmas with an electron temperature several orders of magnitude larger than the ion temperature and gas temperature are referred to as non-thermal or cold plasma; while thermal plasmas feature comparable electron, ion and gas temperature. Thermal plasmas, such as arcs, are destructive and not suitable for a wide variety of applications such as material processing, surface treatment and biomedical sample preparation. On the other hand, non-thermal plasmas have caught much attention due to their potential for these applications including, but not limited to, integrated circuit fabrication.

Plasma research was mostly on low pressure discharges in the past. However, recently atmospheric pressure plasma has been a popular research topic because there is no longer any need for a vacuum pump. This will allow for the plasma manufacturing at lower cost. In addition, the reduced particle mean free path at high pressure makes the plasma and thus the plasma source devices much smaller in size, which may be suitable for portable applications. Besides the plasma sources that this thesis is going to discuss, there are several other prevailing atmospheric pressure plasma sources that are under intensive research. A brief introduction will be given for these plasma sources before the introduction and detailed analysis of the circular and linear microplasma array.

1.1.2 DBD plasma source

DBD plasma source is referred to as dielectric barrier discharge which has been widely used in ozone generation at atmospheric pressure and plasma display panels at moderate pressure (~500 Torr). The common structures are shown in figure 1.1. There are two electrodes known as anode and cathode, and one or two dielectric barriers

serving as an insulating layer covering one of the electrodes to prevent plasma from directly contacting the electrode. This limits the current passing through the discharge to that of the displacement current; these low currents usually prevent arcing of the DBD.

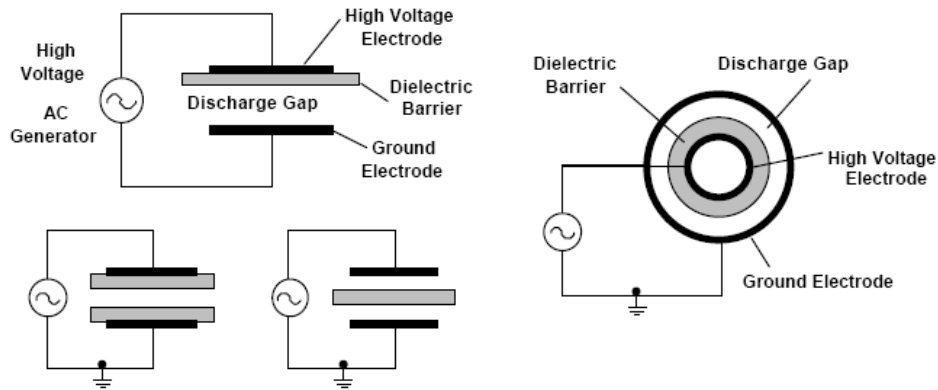


Figure 1.1 Common dielectric barrier discharge electrode configurations. [After Ref 1]

As the voltage on the anode increases, the electric field also increases. When the electric field reaches the breakdown level, plasma is then initiated. Charges are piled up on the dielectric barrier after plasma extinguishes. Ignition may take place at any place where the breakdown criterion is met. DBD plasma is usually operated at kHz or RF frequency range [2].

1.1.3 Plasma jets

Adapted from the DBD geometry, plasma jets can be created using the schematic shown in figure 1.2.

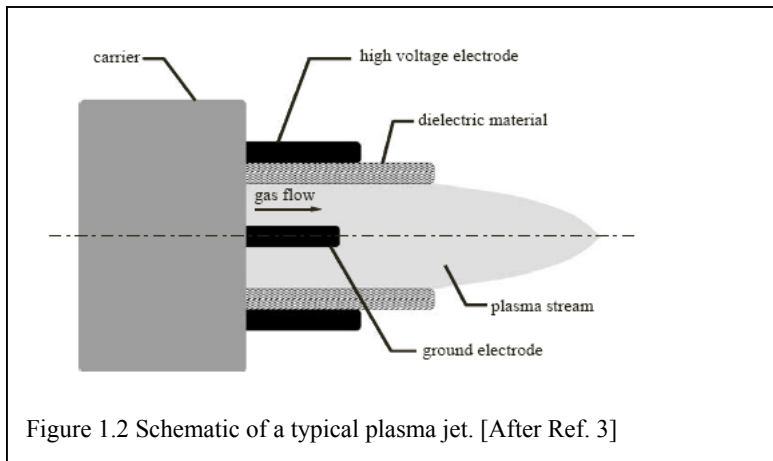


Figure 1.2 Schematic of a typical plasma jet. [After Ref. 3]

Gas is flowing through the concentric dielectric tube. The strong electric field between

the high voltage electrode and ground electrode ignites plasma which then extends along the gas flow to the region outside the tube.

Various gases such as nitrogen [4], helium [5], argon, and mixtures of gases [6], have been used for plasma jet research. Both its temporal [5, 7] behavior and plasma properties using spectroscopic methods [8, 9] have been investigated. High voltage pulses of short duration (~nanoseconds) have been found to produce discharges with less chance for thermal runaway instabilities [10] and can sustain more stable cold plasmas compared with those driven by a continuous sinusoidal power supply [11].

Some of the microplasma jet applications include surface treatment [12] such as thin-film deposition [13] and biomedical sample preparations [14] due to its non-thermal nature. However, these characteristics are not just particular to the plasma jet source. Other atmospheric non-thermal plasma in some common geometries can also be implemented for these applications. So, in this thesis we will introduce two plasma array geometries (circular and linear) to generate microplasma at atmospheric pressure in argon.

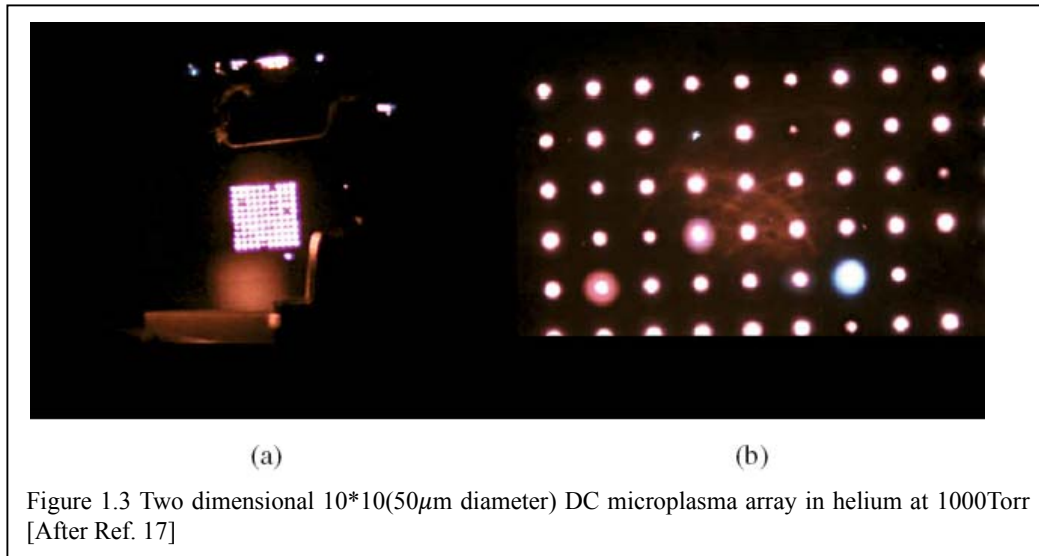
1.1.4 Other plasma sources

Some other atmospheric plasma sources are corona discharge and plasma torch [15]. Both plasma sources are typically operated at DC, but recently there are cases where RF and microwave power supplies are used [16]. Even though the corona discharge is a type of cold plasma, it has some non-uniformity drawbacks because the plasma is ignited at sharp points on the anode electrode. To avoid the transition to a destructive arc, grounded surfaces are placed nowhere near the sharp points. As the spacing between the anode and cathode increases, the electron density decreases dramatically. So the corona is inherently non-uniform. Although similar in structure as the plasma jet, plasma torch is characterized as a thermal plasma source, like arcs, where ion temperature and thus gas temperature are comparable with electron temperature. Due to this feature, the plasma torch is mostly applied in chemical waste destructions, ceramic coating and sintering applications.

1.2 Plasma arrays

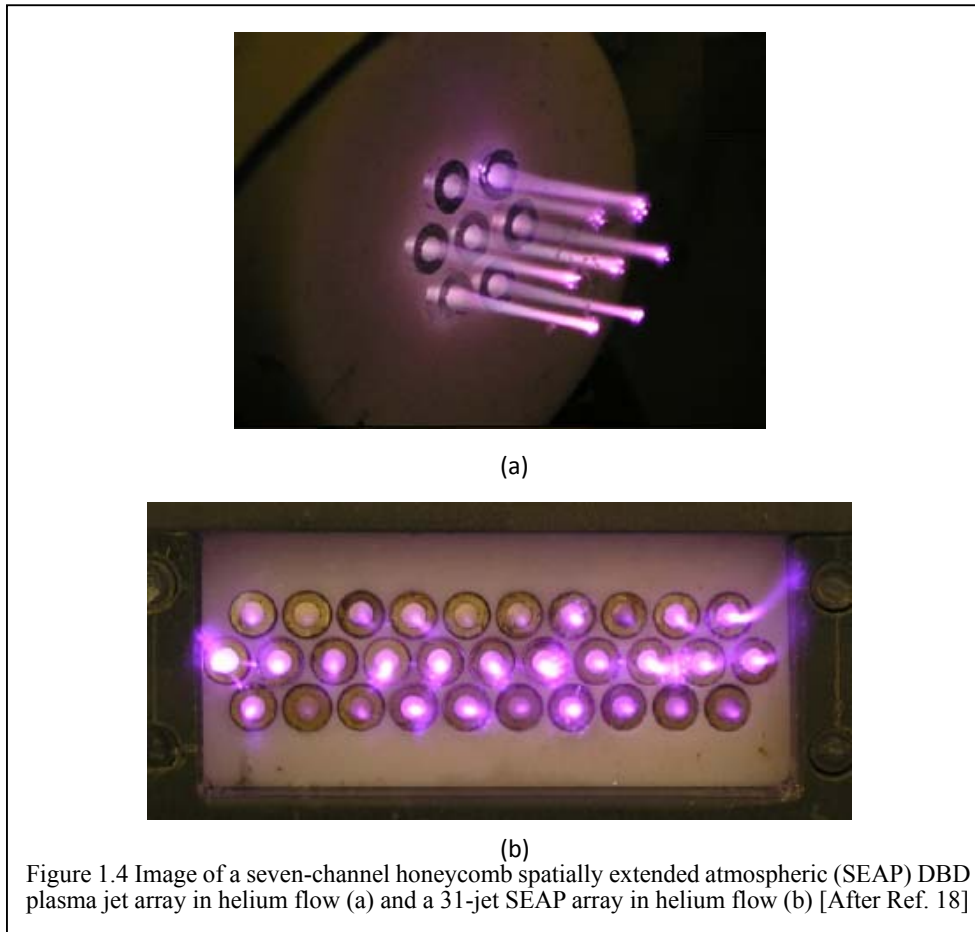
Plasma sources such as DBD plasma jet are considered to be essentially zero

dimensional or known as plasma point source. Higher dimensional plasma arrays could be made by placing multiple plasmas point sources close together to form a particular geometry. The expanding plasma may contact extended areas making it possible for large size processing applications. DC arrays, DBD arrays and plasma jet arrays have been investigated [17, 18]. Specifically, a DC microplasma source has been fabricated using integrated semiconductor processing techniques. The array consists of 100 (10x10) 50 μm to 100 μm diameter cavities as shown in figure 1.3 with microplasmas. In subfigure (a), plasmas in some cavities are not ignited and the close-up subfigure (b) illustrates that for all the ignited plasma, the emission intensities and thus plasma densities vary from cavity to cavity. This is because the substrate, a layer of intrinsic silicon is used as ballast resistor to prevent transition into arc. However, since every resistor is a part of and shares the bulk silicon substrate, the resistance to each individual cell is hard to control. Hence, the challenge is the ballast resistor design, and therefore current DC arrays are usually non-uniform and limited in size.



Plasma jet arrays simply place multiple plasma jets close together to form a 2-D geometry as shown in figure 1.4(a). One of the challenges is the jet-jet interaction which will disturb individual plasmas causing jet convergence, jet divergence and jet extinction as illustrated in figure 1.4(b). The current jet array shown has a 2mm separation and the diameter of each plasma jet is also 2mm. It has been found that excitation frequency less than 10 kHz could help eliminate jet-jet interaction. So, the

operating frequencies of plasma jet type plasma arrays are usually limited between 5 kHz to 10 kHz to ensure uniformity. However, for large area material processing the plasma jet array does not fill all the areas but rather produces seven separated dot plasmas. The region between two jets is insufficient of, if not completely absent of plasmas. Thus, the so-called uniformity is with respect to each individual plasma jet and the prevention of cross talk between any two jets. So, it is typically not appropriate for processing large scale uniform surfaces. In addition, the current largest scale for the plasma jet array is a circle with 21mm in diameter. Compared with this array, the present linear plasma is 90mm long, uniform and suitable especially for roll-to-roll coating applications, as well as RF and potentially microwave operation frequencies and low power consumption.



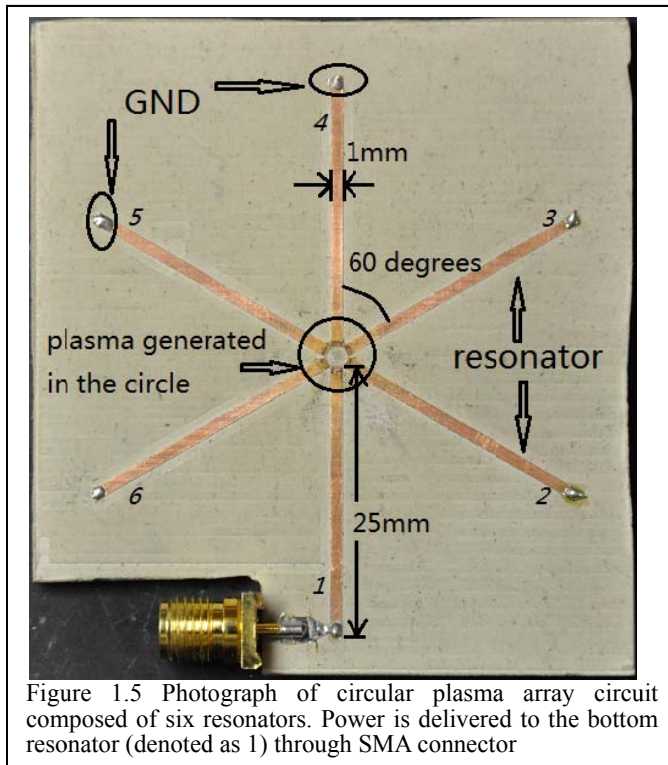
The capacitively coupled microplasmas form a two-dimensional plasma ring and a plasma line in our study. The present linear plasma is moderate in length but has potential for scaling up. These atmospheric pressure microplasma arrays are ignited by

resonators having low power consumption and simple operation features. The generic structures will be shown in the following section that will facilitate understanding detailed analysis that follows.

1.3 Circular and linear arrays' basic structures

In terms of atmospheric pressure plasma arrays, the most typical architectures are rectangles, circles and lines. The quasi 1-dimensional geometries are more easily studied. Thus, in this thesis most effort is dedicated to plasma arrays in the forms of a circle and a line which will be referred to as circular and linear plasma arrays. Firstly, the basic idea will be given about the structure of circular and linear plasma arrays.

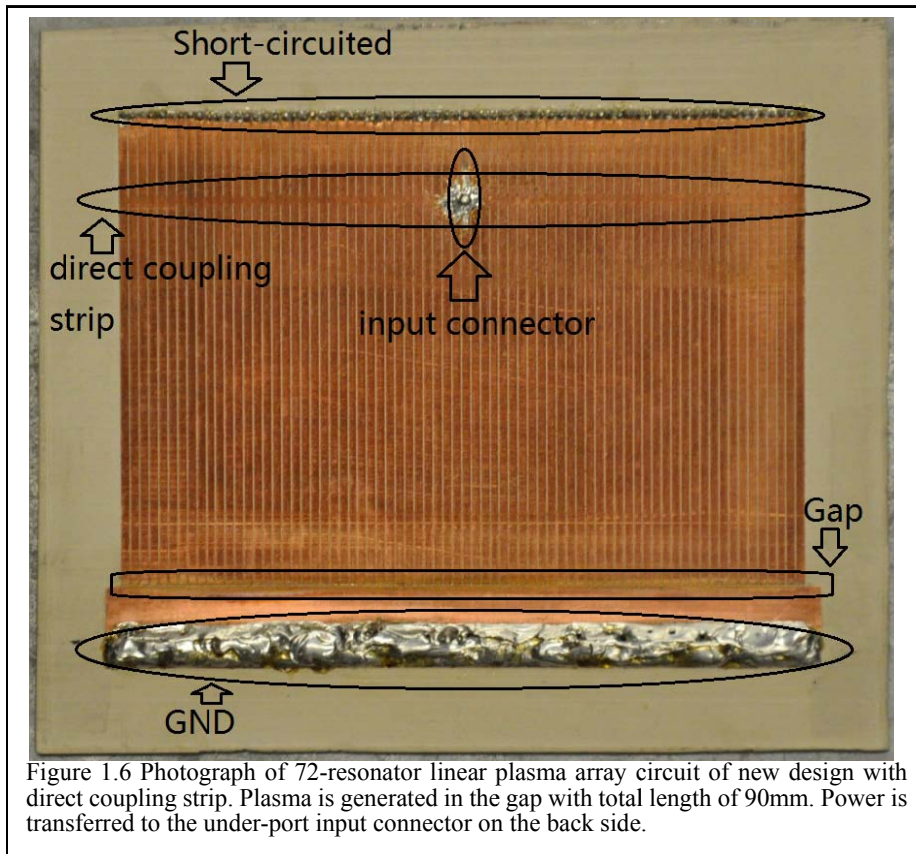
1.3.4 Circular array



The experimental circuit board is first demonstrated in figure 1.5. The circuitry is made of dielectric laminate from Rogers Corp. Simply, a piece of dielectric material with large dielectric constant is clad with copper on both sides. Then a micromilling machine is used to fabricate the circuit, which in this instance is composed of six microstrip line quarter-wavelength resonators. The in-depth physics of microstrip line quarter-wave resonator is discussed in part 2.1.1. One end of the microstrip line is short-circuited to

the ground plane on the back side of the board through a via. The microstrip a quarter-wave in length such that current reaches its maximum at the via and voltage is zero since this point is connected to ground; On the opposite end of the strip, the voltage reaches its maximum and the total conduction current is theoretically zero based on the assumption that the microstrip line is lossless. As the input power increases, the voltage at the tips of each microstrip line will also be enhanced until it reaches the breakdown voltage at which plasma is then initiated. Getting plasma ignited is the first goal, but sustaining it in a uniform shape is another challenge. In the following sections, a technique will be described to keep the circular plasma in a fairly uniform shape.

1.3.4 Linear array



The figure 1.6 above illustrates the structure of a linear array composed of 72 resonators. All of the 72 resonators are placed in parallel and are all connected to the ground plane on the other side of the board through vias at the top end of the photograph, denoted as *Short-circuited* in the picture. There is a 200 micrometer space, denoted as *Gap* in the

figure, between each of the resonator ends and ground, shown as *GND* and this gap is where microplasma is generated. In the later sections, justifications will be provided for why the input node is at the center of the array as well as the function of the direct coupling strip which is connecting all the resonators across the input pin horizontally.

1.4 Research objective

In recent years, intensive research has been being carried out on atmospheric pressure microplasmas. One of the major reasons is that large expensive vacuum systems will no longer be needed in generating plasmas that can be operated in one atmosphere. The current research on plasma arrays is based on the following objectives.

1.4.4 Scientific understanding

We would like to investigate and gain a comprehensive understanding of uniform atmospheric pressure microplasma array ignition conditions and the collective behavior of multiple discharges, especially in these two particular structures. This work also seeks to understand the physics of the power coupling mechanisms and the power distribution at RF and microwave frequency ranges, specifically coupling coefficients and operation modes. The interaction between the microplasma and the microwave circuit, such as plasma instabilities and disturbance brought by the plasma, is also important to understand. A good knowledge of the coupling physics and a method to distribute power uniformly to the microplasmas on each resonator will guide us to develop scaling laws and to fulfill other future work.

1.4.4 Application perspective

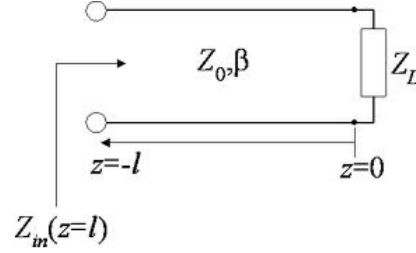
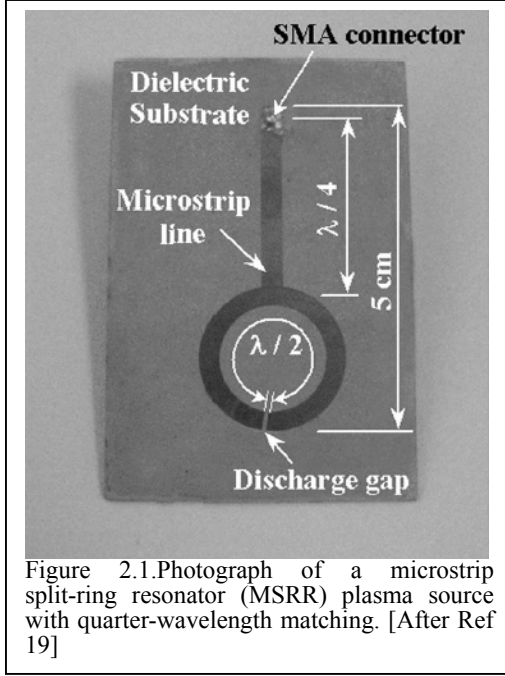
In order to treat temperature sensitive materials such as plastics and biomedical samples, especially without an expensive vacuum pump, a cold microplasma can be used at atmospheric pressure to significantly reduce the system cost and power consumption. The microplasma is a non-equilibrium discharge, unlike the more familiar arc, in which the electrons are hot but the gas remains cooler. Due to its limited size, low power consumption and operating frequency range being close to frequency bands of portable devices such as cell phones, atmospheric microplasma can also be embedded into those portable devices.

2. Theory

In the theory section, we will analyze several models used to predict the behavior of arrays of resonators. First of all, a microstrip quarter-wave resonator model will be derived to show that maximum electric field can be obtained at the resonator tip. Then, the fundamental theory about the power coupling between multiple coupled transmission lines will be discussed in detail, for the linear and circular array. Both the formalism and solutions to the coupled mode theory (CMT) will be provided before any plasma effects are taken into account. Since the CMT representation model for the linear array is more straightforward than the circular array, circular array CMT analysis will be carried out after the linear array. Finally, the physical model of the coupling coefficient between two resonators will be demonstrated.

2.1 Quarter-wave resonator model

The original concept of using a microstrip resonator to generate plasma comes from the microstrip split-ring resonator (MSRR) microplasma source. [19] The MSRR is a half wave resonator in a ring shape as shown in figure 2.1. The voltages on the tips of the discharge gap are 180-degrees out of phase. This location is where the electric field becomes large enough for most gases to reach breakdown level inside the gap. Using a split-ring, less power is needed to start plasma than from a breakdown voltage that is simply relative to ground.



The split-ring geometry, however, is not easy to fabricate in arrays. A linear microstrip resonator is therefore examined next. The theoretical model of the quarter-wave resonator is shown in figure 2.2, where Z_0 , Z_L and Z_{in} are the characteristic impedance, load impedance and input impedance respectively; $\beta = \frac{2\pi}{\lambda}$ is the wave number. The input impedance of this lossy transmission line is given as

$$Z_{in} = \frac{V(-l)}{I(-l)} = Z_0 \frac{Z_L + Z_0 \tanh \gamma l}{Z_0 + Z_L \tanh \gamma l} \quad (2.1) \quad [20]$$

where $\gamma = \alpha + j\beta$ is the complex propagation constant of the transmission line and α represents wave attenuation. Now, if we have an open circuit as the load ($Z_L = \infty$) which applies to our case, equation 2.1 becomes

$$\begin{aligned} Z_{in} &= Z_0 \coth(\alpha + j\beta)l \\ &= Z_0 \frac{1 + j \tan \beta l \tanh \alpha l}{\tanh \alpha l + j \tan \beta l} \\ &= Z_0 \frac{\tanh \alpha l - j \cot \beta l}{1 - j \tanh \alpha l \cot \beta l} \end{aligned}$$

Then, we assume small attenuation ($\tanh \alpha l \approx \alpha l$), and a small deviation from the resonant frequency ($\beta l = \beta \left(\frac{\lambda}{4} + \Delta l \right) = \frac{\pi}{2} + \frac{\pi \Delta \omega}{2\omega_0}$)

Then, $\cot \beta l = \cot \left(\frac{\pi}{2} + \frac{\pi \Delta \omega}{2 \omega_0} \right) = -\tan \frac{\pi \Delta \omega}{2 \omega_0} \approx -\frac{\pi \Delta \omega}{2 \omega_0}$

Finally giving, $Z_{in} = Z_0(\alpha l + j \frac{\pi \Delta \omega}{2 \omega_0}) / (1 + j \alpha l \frac{\pi \Delta \omega}{2 \omega_0})$

In the denominator, since $|j \alpha l \frac{\pi \Delta \omega}{2 \omega_0}| \ll 1$ for any small frequency deviation,

$Z_{in} = Z_0(\alpha l + j \frac{\pi \Delta \omega}{2 \omega_0})$. Compared with the RLC series resonant circuit where

$$Z_{in} = R + 2jL\Delta\omega = R + 2jQR \frac{\Delta\omega}{\omega_0},$$

We can obtain $R=Z_0\alpha l$; $L=\frac{\pi Z_0}{4\omega_0}$ and $C = \frac{1}{\omega_0^2 L}$; $Q = \frac{\beta}{2\alpha}$ for the corresponding lumped element series resonator model.

The single quarter-wavelength microstrip resonator is presented in the following figure 2.3. The microstrip line is 62mm long and 1mm wide with the end on the right connected to the ground plane on the back side of the board and the opposite end open-circuited. Input power is delivered by an SMA (Sub-Miniature version A) connector through a taper to the quarter-wavelength resonator. The taper position is chosen to be close to the short-circuited end for the reason that the overall impedance seen by the input connector is matched to the characteristic power source impedance (50ohms) to ensure maximum power delivery efficiency. In the case of the MSRR, the input impedance presented to the input connector after plasma is initiated follows this equation:

$$Z_{in} = Z_0 \left\{ \frac{Z_0 + \left(\frac{Z_p}{2}\right) \tanh(jkl_1)}{(Z_p/2) + Z_0 \tanh(jkl_1)} + \frac{Z_0 + \left(\frac{Z_p}{2}\right) \tanh(jkl_2)}{(Z_p/2) + Z_0 \tanh(jkl_2)} \right\} [21]$$

l_1 and l_2 are the microstrip line length from the input node to the either end and Z_p is the microplasma impedance. Adapted from the equation above, the input impedance of the single quarter-wavelength resonator is in the form of:

$$Z_{in} = Z_0 \left\{ \frac{Z_0 + Z_p \tanh(jkl_1)}{Z_p + Z_0 \tanh(jkl_1)} + \coth(jkl_2) \right\}$$

l_1 and l_2 denote the microstrip line length from the input node to the open-circuited end and short-circuited end respectively. Hence, in the presence of plasma, the input impedance Z_{in} will deviate from the pre-matched value Z_0 in both real and imaginary

components due to the complex form of plasma impedance Z_p . Therefore, the quality factor Q and reflection coefficient S_{11} will be degraded. More detailed analysis will be provided in section 2.8.8 about plasma loading effect.

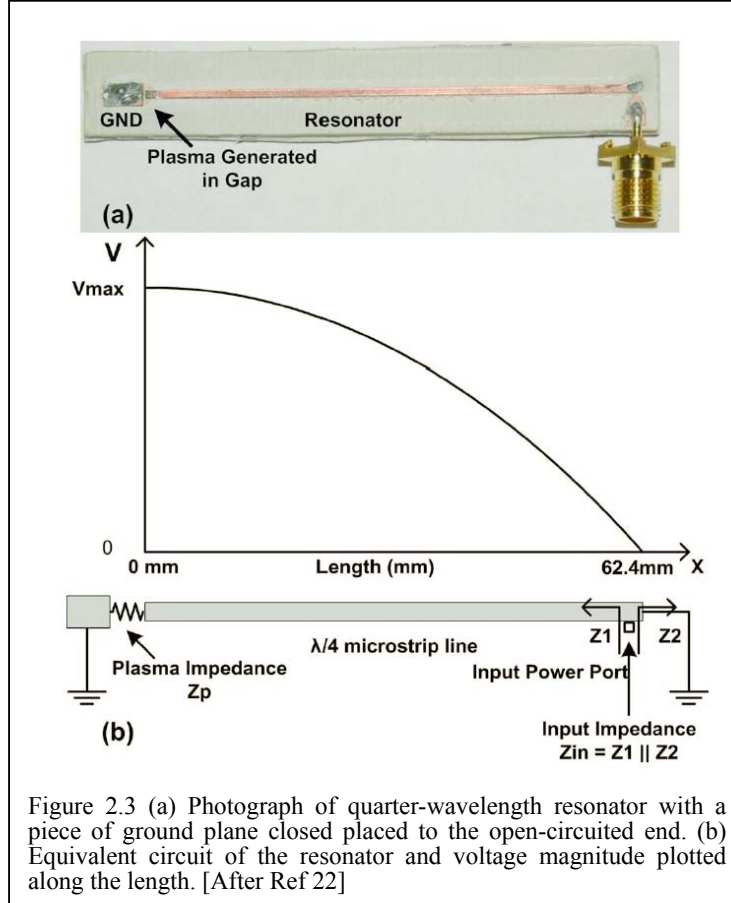


Figure 2.3 (a) Photograph of quarter-wavelength resonator with a piece of ground plane closed placed to the open-circuited end. (b) Equivalent circuit of the resonator and voltage magnitude plotted along the length. [After Ref 22]

2.2 Coupled mode theory introduction

Now that we have seen the structure of both the circular array and linear array, notice that in both cases only one input connector is used for power delivery but plasma will be present at all resonator tips. Thus, there should be an efficient energy sharing mechanism among the resonators which is the essence of these designs. Ideally, we would like uniformly distributed power going to each resonator. However, for the simplest example where two quarter-wave resonators are in parallel, we observed that two of the four ends are open-circuited and the other two are short-circuited. There is not much flexibility to design the load impedance such that exactly half of the power is coupled from the input resonator to the other. How much power is transmitted from the master resonator to the slave resonator is substantially dependent on the coupling

strength between them. Therefore, we will now introduce a coupling theory borrowed from optics called coupled mode theory (CMT) to help us understand and predict the power distribution on these arrays.

2.2.1 CMT differential equation matrix interpretation

The coupled mode theory [23] which has been used to model the power distribution among resonators at microwave frequency range and higher has the formalism shown in the formalism (2.1) below.

$$\dot{a}_m(t) = (i\omega_m - \Gamma_m)a_m(t) + \sum_{n \neq m} i\kappa_{mn}a_n(t) + F_m(t) \quad (2.1)$$

The variables $a_m(t)$ are defined such that the power on the resonator m is equal to $|a_m(t)|^2$; ω_m is the natural resonant frequency of resonator m without coupling effect and Γ_m is the intrinsic decay rate due to radiation and dielectric losses on the microstrip line. $\kappa_{mn} = \kappa_{nm}$ are the coupling coefficients that describe the rate of power transfer between resonator m and n . $F_m(t)$ is the driving force, which in our case is the input power. Therefore, the linear equations above indicate that the energy stored in a resonator will increase due to the forcing function $F_m(t)$ and coupling from neighboring resonators and decrease due to the damping term Γ_m . The numerical value of the coupling coefficients between two arbitrary resonators must be determined separately for a specific geometry as follows. Two equations can be derived by the formalism given in (2.1) for two parallel coupled identical resonators. They could be simplified by having F_m equal zero based on the assumptions that these two resonators are at resonance and the solution is at steady state. The solution results in a splitting of the single resonant frequency into two resonant frequencies (f_L and f_H) due to the coupling between them. f_L is the resonant frequency lower than the natural resonant frequency and f_H is the one higher. CMT then tells us that the coupling coefficient between any two resonators can be determined, by direct measurement or by electromagnetic modeling, from half the resonant frequency difference, specifically

$$\kappa = \frac{f_L - f_H}{2} \quad (2.2)$$

2.2.2 Generic CMT linear equation set for 5 resonators

As a specific example of CMT, consider the case of five resonators. We restrict the response to sinusoidal steady-state and, after some manipulation, the generic matrix representation of the CMT equations is listed in equation 2.3 for the homogeneous linear equation set. We assume that the natural resonant frequency for all the resonators is identical and equal to ω_0 because all the resonators have the same length.

$$\begin{bmatrix} \omega_0 - \omega + i\Gamma_0 & k_{12} & k_{13} & k_{14} & k_{15} \\ k_{21} & \omega_0 - \omega + i\Gamma_0 & k_{23} & k_{24} & k_{25} \\ k_{31} & k_{32} & \omega_0 - \omega + i\Gamma_0 & k_{34} & k_{35} \\ k_{41} & k_{42} & k_{43} & \omega_0 - \omega + i\Gamma_0 & k_{45} \\ k_{51} & k_{52} & k_{53} & k_{54} & \omega_0 - \omega + i\Gamma_0 \end{bmatrix} \begin{bmatrix} a_1 \\ a_2 \\ a_3 \\ a_4 \\ a_5 \end{bmatrix} = \begin{bmatrix} 0 \\ 0 \\ 0 \\ 0 \\ 0 \end{bmatrix} \quad (2.3)$$

κ_{mn} is the coupling coefficient from resonator n to resonator m. So, the n^{th} row in the coupling coefficient matrix in 2.3 represents the power coupling from other resonators to the n^{th} resonator. Once we know the generic representation of CMT, we will show the same equation set for the linear array model with some minor modification.

2.2.3 Linear array CMT matrix representation

Starting from the generic linear equation matrix representation, we will do some minor modification to the linear equation set for the linear array based on the geometric condition particular to the array: the coupling coefficients κ_{mn} will be ignored for $|m - n| > 5$. This assumes that we neglect the power coupling effect when two resonators are separated far part. With simulation results, we define that coupling of resonators with a distance equivalent to more than 5 resonators can be ignored which is 5.25mm. Therefore, for each resonator there are 8 resonators to couple power from, 4 on the left and 4 on the right. Exceptions are for the 4 resonators on the left and right edges where there are fewer than 4 resonators on one of the two sides. The coupling coefficient matrix could be simplified by the fact that the coupling between two resonators is the same as long as the separation remains the same regardless of the relative position of these two resonators in the linear array. Specifically, it means that $\kappa_{1,2} = \kappa_{2,3} = \kappa_{3,4} = \dots = \kappa_{71,72}$ for the coupling of two neighboring resonators;

$\kappa_{1,3} = \kappa_{2,4} = \kappa_{3,5} = \dots = \kappa_{70,72}$ for the coupling of every other resonator and etc. As assumed in section 2.2.1, the condition that $\kappa_{mn} = \kappa_{nm}$ will be applied in solving the equation set as well. With these simplifications taken into account, the linear array CMT linear equation set is shown in equation 2.4.

$$\begin{bmatrix} \omega_0 - \omega + i\Gamma_0 & \kappa_{12} & \kappa_{13} & \dots & 0 \\ \kappa_{12} & \omega_0 - \omega + i\Gamma_0 & \kappa_{12} & \dots & 0 \\ \kappa_{13} & \kappa_{12} & \omega_0 - \omega + i\Gamma_0 & \dots & 0 \\ \vdots & \vdots & \vdots & \ddots & \vdots \\ 0 & 0 & 0 & \dots & \omega_0 - \omega + i\Gamma_0 \end{bmatrix} \begin{bmatrix} a_1 \\ a_2 \\ a_3 \\ \vdots \\ a_{72} \end{bmatrix} = \begin{bmatrix} 0 \\ 0 \\ 0 \\ \vdots \\ 0 \end{bmatrix} \quad (2.4)$$

To obtain the coupling coefficients $\kappa_{12}, \kappa_{13}, \kappa_{14}$ and κ_{15} which are formulated by equation 2.2, simulations have been carried out to calculate the resonant frequencies splitting for pairs of resonators separated by distances of 0.25mm, 1.5mm, 2.75mm and 4mm respectively since each resonator is 1mm wide and the gap between two resonators is 0.25mm. Using HFSS (Ansoft Corporation's High Frequency Structure Simulator) to simulate the resonant frequency splitting for pairs of resonators gives the results that $\kappa_{12}, \kappa_{13}, \kappa_{14}$ and κ_{15} are 40MHz, 31MHz, 18MHz, and 9MHz. Thus, we will use these values to calculate the solution to the linear equation set in 2.4. Now that we have the CMT model, the next step is to solve it and get the relative power distribution on the array. If the distribution is uniform, it is more likely to create a uniform plasma along the array gap. Unfortunately, it will be shown that the coupling is not strong enough to transfer power uniformly all the way to the edge of the array, which is about 45mm away. So, a direct coupling method will then be introduced to enhance power sharing in the later sections.

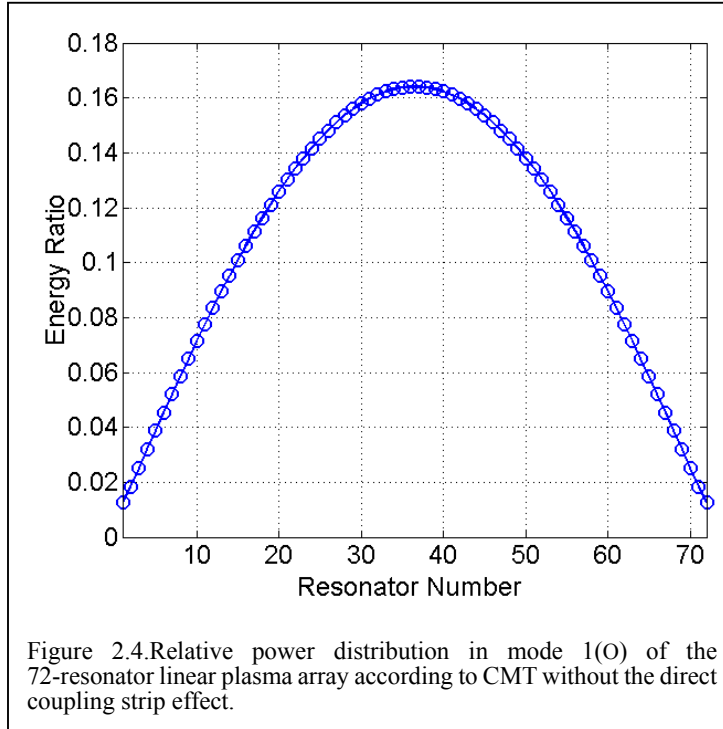
2.2.4 Linear array equation set solution

For the time being, all the resonators are assumed to operate at the same resonant frequency ω_0 before plasma is ignited. This is the case for the experiment due to the identical length strips and thus the uniform damping factor Γ_0 , so long as there is not too much discrepancy between resonators when fabricating the circuit. After estimating

the energy loss term from vector network analyzer measurements of quality factor (Q) to be $\Gamma_0 \sim 5\text{MHz}$, we have determined all the parameters and can solve homogeneous linear equation set. The way to solve the homogeneous equations is by getting the eigenvalues of the coefficient matrix and then finding the eigenvector particular to each eigenvalue. According to CMT, every eigenvalue-eigenvector pair is a valid mode for the array to operate in. The eigenvector represents one possible energy distribution on the resonators of the array. In theory, the number of resonators equals the number of resonant frequencies possible for the whole array due to coupling and resonant frequency splitting. An additional resonator will add one more mode to the array in which the array can resonate. However, as will be discussed in detail later in section 2.2.9 and verified by simulation and measurement, lower modes corresponding to lower resonant frequencies have strong resonance on the reflection coefficient spectrum (S_{11} plot) which means less input power reflection and these modes are more recognizable from neighboring modes (resonant frequencies). Higher modes tend to be close to each other in frequency and exhibit more reflection, thus these resonant frequencies become indiscernible from each other on the power absorption spectrum and difficult to investigate experimentally.

In this section, only the relative power distribution in the first mode of the 72-resonator array is given in figure 2.4 with circle markers. Higher mode solutions will be analyzed in section 2.2.9. The power for each resonator is given in the form of $|a_m(t)|^2$. From the figure, it is easy to tell that the power going to the center resonators is about 10 times as much as the power delivered to the side ones. This amount of power difference is too considerable to ensure uniform plasma. In addition, as will be estimated in the circular array, simulations and experiments have also proven that, in the presence of microplasma, using CMT alone may cause power to go to the input resonator much more than any other resonators and thus result in non-uniformity and sometimes instability. [5] Furthermore, this significant power variation can only be alleviated from improving the CMT coupling coefficients by moving the resonators closer to each other. The practical gains in power uniformity and plasma stability, however, are limited since

the practical separation between resonators is restricted to 0.25mm due to the available fabrication machine.



2.2.5 The improvement of direct coupling strip on the energy distribution of the linear array

The huge center-to-edge power difference from the CMT linear equation set solution requires a better mechanism to transmit power to the edges. Thus, a direct coupling path has been added to the linear array which intersects the input pin with a connection to each resonator as illustrated in figure 1.2. In this new coupling scheme, input power can propagate not only vertically along the input resonator, but also horizontally along the direct coupling strip path. As will be confirmed by HFSS simulation results of electric field distribution in section 3.2, the direct coupling strip has the effect of substantial enhancement of coupling among resonators. In terms of the prediction by CMT, for the arrays with the same number of resonators, the direct coupling strip reinforces the coupling coefficients so that energy on each resonator decays down much more slowly towards the edges compared with the structure without the DCS. However, energy still decays, eventually to a level that is not sufficient to generate plasma. Therefore, the

improvement from the DCS is not definitive for infinite long array but certainly will produce a more uniform plasma for a reasonable scale.

The linear array model has evolved from a simple CMT model to the combination of CMT and a direct coupling strip. Later sections will show that the direct coupling strip improves the performance of the array significantly in both simulation and experiments. Before we show these results, the other CMT model for circular arrays will be analyzed. Due to its symmetric physical structure, we will find a symmetric coupling coefficient matrix and this effect results in the intrinsically uniform power distribution without the addition of any direct coupling path.

2.2.6 Circular array CMT matrix representation

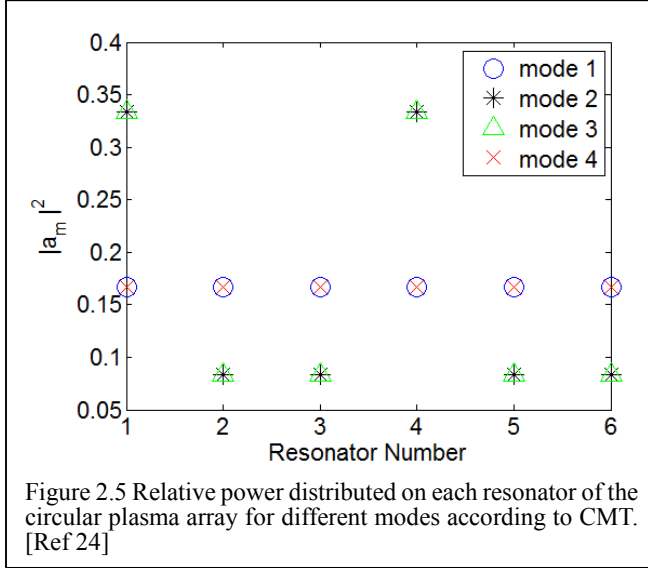
The homogeneous linear equation set of the circular array is different from that of the linear array due to the particular symmetric geometry of the circular array. From figure 1.1, every resonator sees the same array structure, specifically one resonator every 60 degrees. Compared with the linear array case where resonators on the two edges can only couple power to one side, the circular array breaks down this asymmetry. Therefore, the coupling coefficient matrix can be further simplified thanks to the symmetry. In particular, if we assume resonator 1 is the one to which the power source is connected and resonator 2, 3, 4, 5, 6 are labeled in the counterclockwise direction as denoted in figure 1, then $\kappa_{12}, \kappa_{13}, \kappa_{14}$ are the coupling coefficients between resonator 1 and 2; resonator 1 and 3 and resonator 1 and 4 respectively. For the same reason of constructing the linear array equation set, we have $\kappa_{12} = \kappa_{23} = \kappa_{34} = \kappa_{45} = \kappa_{56}$. Moreover, the symmetry gives $\kappa_{56} = \kappa_{61}$ which is absent in the linear array matrix. So, following the same logic, we define κ_{12} to be the coupling coefficient of every two neighboring resonators; κ_{13} to be the coupling coefficient of every other resonators separated by 120degrees and κ_{14} to be the coupling coefficient of every two resonators on the opposite side (180 degrees). Having built up the CMT linear equation set of the circular array in equation 2.6 below, we equate the determinant of the coupling coefficient matrix to zero to find a non-trivial solution.

$$\begin{bmatrix}
\omega_0 - \omega + i\Gamma_0 & k_{12} & k_{13} & k_{14} & k_{13} & k_{12} \\
k_{12} & \omega_0 - \omega + i\Gamma_0 & k_{12} & k_{13} & k_{14} & k_{13} \\
k_{13} & k_{12} & \omega_0 - \omega + i\Gamma_0 & k_{12} & k_{13} & k_{14} \\
k_{14} & k_{13} & k_{12} & \omega_0 - \omega + i\Gamma_0 & k_{12} & k_{13} \\
k_{13} & k_{14} & k_{13} & k_{12} & \omega_0 - \omega + i\Gamma_0 & k_{12} \\
k_{12} & k_{13} & k_{14} & k_{13} & k_{12} & \omega_0 - \omega + i\Gamma_0
\end{bmatrix}
\begin{bmatrix}
a_1 \\
a_2 \\
a_3 \\
a_4 \\
a_5 \\
a_6
\end{bmatrix}
=
\begin{bmatrix}
0 \\
0 \\
0 \\
0 \\
0 \\
0
\end{bmatrix} \quad (2.6)$$

The vector $[|a_1|^2 \ \dots \ |a_6|^2]^T$ is defined to be the power delivered to each resonator. Using HFSS to simulate the resonant frequency splitting for pairs of resonators, namely resonator 1 and 2; 1 and 3; 1 and 4 by modeling these pairs with other resonators absent and then applying equation 2.2, we could obtain the coupling coefficients to be 26MHz, 5MHz and 5MHz for κ_{12} , κ_{13} and κ_{14} respectively.

2.2.7 Circular array equation set solution

Applying the coupling coefficients into equation 2.6 for the circular array and equating the determinant of the matrix to zero to get eigenvalues and corresponding eigenvectors, we find the eigenvectors, and thus power distribution as shown in figure 2.5. In the figure, only the first four modes are shown. This is because only four resonant frequencies have been observed in both the simulation result and experimental measurement for the same reason mentioned in the linear array that higher modes are nearly degenerate, have strong reflection and weak resonance, thus they grow so close to each other that they overlap and appear as one resonance on the spectrum. Details of higher modes will be discussed in the section 2.2.9. From figure 2.5, CMT predicts a uniform power distribution on the circular array prior to the ignition of plasma. Mode 1 corresponds to the eigenvector at the lowest resonant frequency of the system. The fourth mode is also a uniform power distribution among the resonators. For mode 2 and 3, most of the power goes to the first and fourth resonators, namely the input resonator and the one that is directly opposite. Hence, it is preferable to generate and operate the plasma in the first or fourth mode for uniform power distribution.

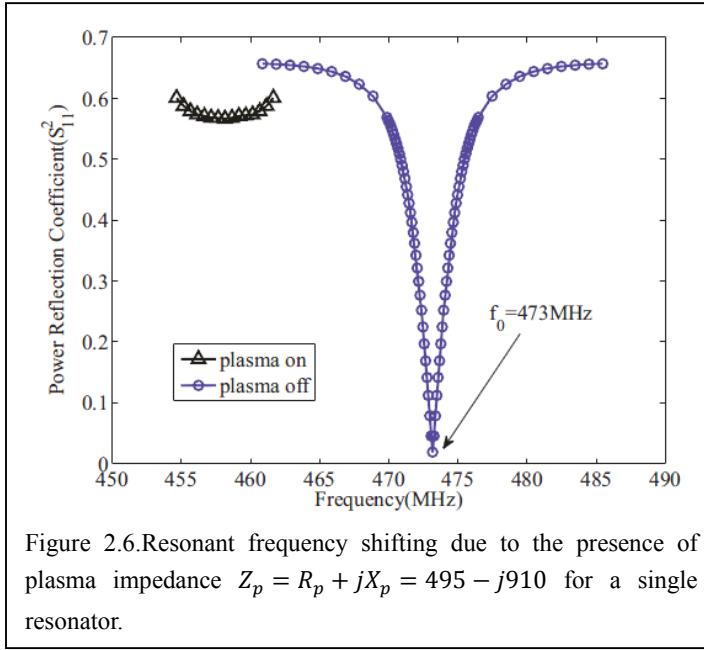


Despite the CMT-predicted power distribution uniformity of circular arrays, capacitive plasma impedance will result in substantial perturbation to the power distribution. So, it is worthwhile to estimate the effect of plasma on the circular array using the CMT model. In the following section, the plasma perturbation effect will first be modeled as an RC circuit, and modification will be done to the coupling coefficient matrix accounting for the plasma effect. Solving the modified equation set will show the new power distribution caused by the plasma. Unfortunately, it will be shown that the disturbance brought by plasma will eventually cause instability.

2.2.8 CMT estimate of the plasma effect on the circular array

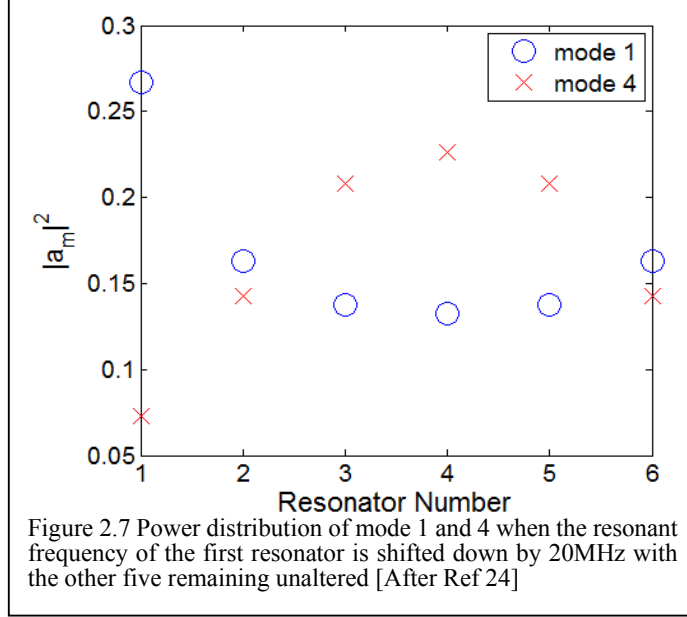
Previous work [21] has shown that microplasma can be modeled as a resistor representing collisional electrons in the bulk plasma. This resistive region is sandwiched by two capacitances due to the electron-depleted plasma sheath regions. The resulting circuit model for the microplasma is $Z_p = R_p + jX_p$. As has been experimentally confirmed, once the microplasma is generated, the parasitic capacitive loading of a resonator by the microplasma sheath will shift down its resonance frequency about 15 MHz below its natural operating frequency ($f_0 = 473 \text{ MHz}$) as demonstrated in figure 2.6 [25]. The microplasma's resistance deteriorates the quality factor Q of the resonator represented as more power reflection and shallower and wider resonance in the figure (by enhancing the damping factor Γ). Although the exact

resonant frequency shift varies for different microplasma sizes and geometries, a typical value is -20MHz.



To investigate the plasma effect on power delivery to each resonator of the circular array, one may artificially reduce ω_1 (the resonant frequency of the input resonator) to model the presence of plasma on resonator 1. Figure 2.7 shows the solved eigenvectors of both mode 1 and 4 with the plasma effect of -20MHz deliberately introduced to the first resonator of the circular CMT matrix. In the 1st mode, CMT shows that more power is stored in the first resonator and less power is delivered to the other ones, with a minimum power appearing on the resonator 4. Until now, the steady-state plasma effect has been modeled to be a fixed-value resistor and capacitor in series. However, this is not the case for the plasma before stabilization. In particular, this power unbalance causes the first resonator to generate more intense plasma in the 1st mode, expanding the area of the plasma sheath along the microstrip line, which increases the plasma volume and thus the additionally enhances effective capacitance and further disrupts the uniform distribution of power among the resonators of the array by letting more power go to the first resonator. Therefore, one step leads to the next and this process behaves like a positive feedback loop where the power and also the plasma

would go to extremes if no further action is taken to restrict the plasma volume expansion. Fortunately, as will be pointed out and discussed in section 4, dielectric plasma limiters have been verified to restrict the overlapping electrode area where plasma could appear and thus prevent this type of non-uniformity.



2.2.9 Higher modes of circular and linear arrays

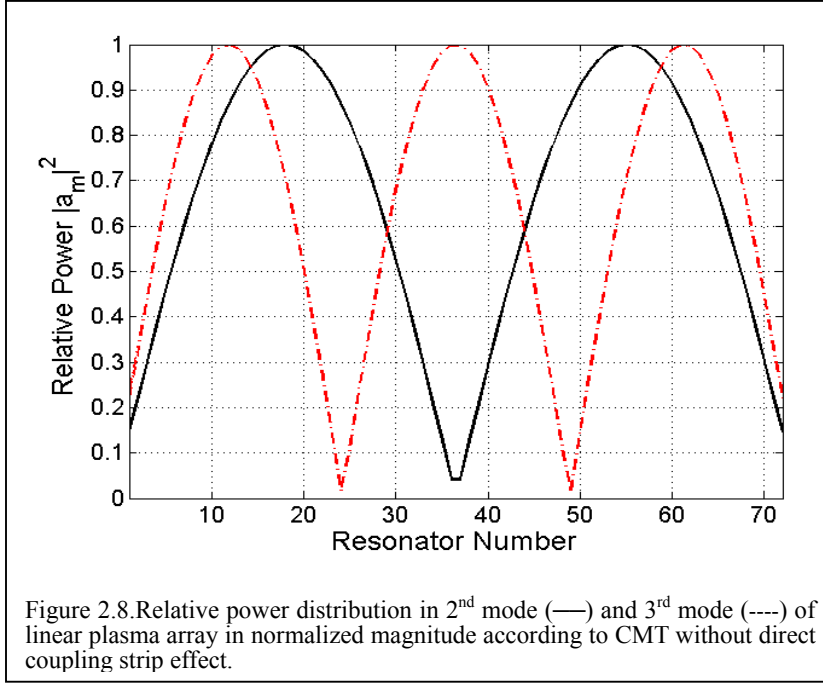
According to CMT, the number of resonant frequencies should be equal to the number of resonators of the whole system. The lowest resonant frequency is defined to be the first mode and next resonant frequency is second mode and etc. That is to say besides the first mode, there are higher modes in which the plasma arrays can operate with different power distributions and thus different plasma patterns than the first mode. In figure 2.5, power distributions to all four modes are presented for the circular array. Theoretically, there should be six resonant frequencies but simulation results and experimental measurement confirm that there are only four discernible resonant frequencies because 5th and 6th mode are either too close to 4th mode to be recognized or very small portion of the input power is absorbed and most power is reflected due to poor impedance matching particularly for these two modes. In 2nd mode and 3rd mode of figure 2.7, power is not uniformly allocated even without plasma effect, so this will restrict plasma to be only on resonator 1 and 4 and plasma effect may even make this

worse. This is why mode 2 and 3 are not preferable to start the plasma in the circular array.

The linear array has the same feature as a circular array: higher modes, especially much higher than the 4th mode, are close to each other thus becoming indistinguishable. Furthermore, the input impedance in simulations and experiments is tuned to match 50 ohms at the first mode since the first mode is desired to generate uniform plasma for the reasons given below. Therefore, as modes become higher, the impedance mismatch grows severely and reflection coefficients at these modes become deteriorated. Nevertheless, in section 3, it will be shown that it is in contrary to the case with direct coupling strip where the spectrum spacing between every two resonant frequencies remains almost constant until considerable impedance mismatch prevails, the reflection becomes damped and the array has very weak resonance and no longer behaves like a resonator.

In the linear array, the 2nd and 3rd eigenvectors corresponding to the eigenvalues of homogeneous CMT result in the 2nd mode and 3rd mode as illustrated in figure 2.8. The 2nd mode is in solid black line with two peaks while the 3rd mode is shown as the dotted red curve with three maxima. For both 2nd and 3rd mode, the power distribution experiences minima at both edges as with the 1st mode, and there are one and two minima in the center part respectively. These intrinsic power minima prohibit any uniform operation in these higher modes. On the other hand, these higher modes can be superimposed with the first mode to sustain more uniform plasma than simply using a single mode. [22] With the direct coupling strip, power increases at the edges of the array since the particular solution predicts that power increases approaching the edges. Therefore, we would expect the combination of power distribution resulting from CMT and the direct coupling strip to be CMT-like at the center and a power increase towards the ends. This will be demonstrated and verified by simulation and experiment results in section 3 and 4. As in CMT with an additional direct coupling strip, the power still experiences one or multiple minima in the center part, so single higher mode operation is not appropriate for having a uniform plasma. Furthermore, what is hidden in figure

2.8 is that the relative power is plotted in $|a_m(t)|^2$, but $a_m(t)$ has phase information. For example, in mode 2, the left portion of the array is 180 degrees out of phase with the right portion and the power minima is located in the position of the phase transition; in mode 3, left and right parts are out of phase with the center part. This effect will be illustrated using surface current plots from simulations in a following section.



So far, the coupling coefficient has been vague in terms of its physical meaning. So, the following section is going to give a physical explanation of the coupling coefficients and derive the coupling between two resonators using a simple lumped LC model. Although the definition is slightly different from the coupling coefficient in CMT because it has the unit of frequency in CMT, the physics behind the model should be the same.

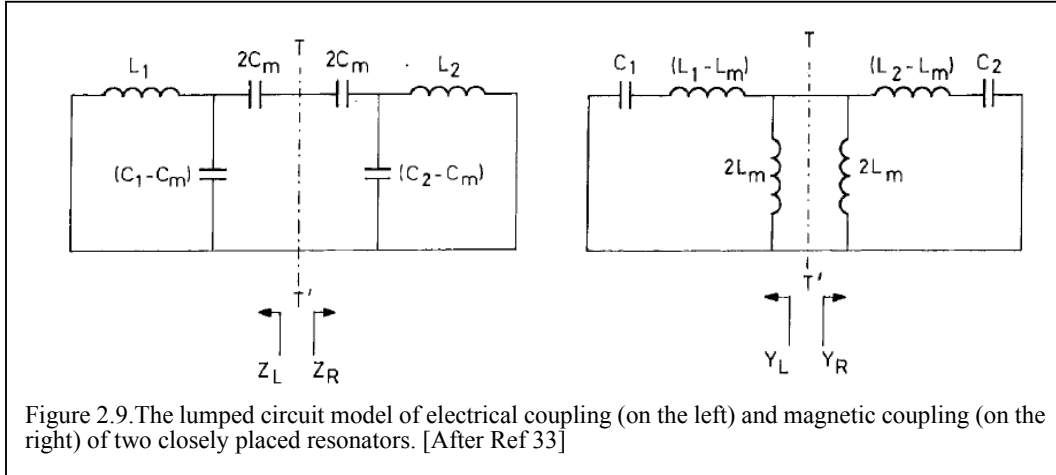
2.3 Theoretical magnetic and electric coupling mechanisms and coupling coefficient modeling.

The power coupling between resonators is a key point in generating uniform plasma. It is claimed that there are essentially two mechanisms engaged in energy coupling, namely the electrical coupling and magnetic coupling. The electric field has its maximum at the tips of each resonator; while the magnetic field has its maximum near

the vias connected to the ground plane where resonator's current is maximized. Hence, it is believed that electric coupling primarily takes place at resonator tips and the vias connected to ground give rise to magnetic coupling. As a matter of fact, these two fundamental coupling mechanisms have been used in a variety of applications such as microwave couplers, filters and etc. [26-32] Theoretically, the detailed analysis of couplings between two coupled microwave resonators has been previously studied and summarized. [33, 34] In general the physical coupling between two resonating objects is due to the electric or magnetic field shared by these two objects. The ratio of coupled energy to the energy stored is given as K in the equation 2.7. Although it is also named coupling coefficient, it differs from the coupling coefficient in the CMT because K accounts for the energy ratio, has an arbitrary unit and is usually used for coupling between two or multiple resonators that are driven at resonance individually; while κ is particular to the CMT, has a frequency unit and is used for coupling between multiple resonators driven at the same single resonant frequency as a system.

$$K = \frac{\iiint \varepsilon \mathbf{E}_1 * \mathbf{E}_2 dv}{\sqrt{\iiint \varepsilon |\mathbf{E}_1|^2 dv \times \iiint \varepsilon |\mathbf{E}_2|^2 dv}} + \frac{\iiint \mu \mathbf{H}_1 * \mathbf{H}_2 dv}{\sqrt{\iiint \mu |\mathbf{H}_1|^2 dv \times \iiint \mu |\mathbf{H}_2|^2 dv}} \quad (2.7)$$

The equation 2.7 above gives the general formula of the coupling between two resonating objects where the volume integrals are in the regions with effective permittivity ε and permeability μ . The first term on the right hand side represents the electric coupling and the second term is the magnetic coupling. Suppose the two resonators have natural resonant frequencies of ω_{01} and ω_{02} respectively, before they are put closely together and any coupling becomes significant. Then the coupling coefficients can be determined and represented by four characteristic resonant frequencies, ω_{01} , ω_{02} , ω_1 and ω_2 . The last two are the resonant frequencies when the two resonators are close to each other.



The two circuit schematics in figure 2.9 are the lumped element model for electric coupling and magnetic coupling, characterized by the mutual capacitance and mutual inductance denoted as C_m and L_m respectively. At resonant frequency, impedance/admittance on the left side of the dotted line interface (TT') should be equal to the negative of the impedance /admittance on the right side so that all and reactances cancel out.

$$\frac{1}{j\omega C_m} + \frac{j\omega L_1}{1 - \omega^2 L_1 (C_1 - C_m)} + \frac{j\omega L_2}{1 - \omega^2 (C_2 - C_m)} = 0 \quad (2.8)$$

$$\frac{1}{j\omega L_m} + \frac{j\omega C_1}{1 - \omega^2 C_1 (L_1 - L_m)} + \frac{j\omega C_2}{1 - \omega^2 (L_2 - L_m)} = 0 \quad (2.9)$$

Both equation 2.8 and 2.9 give the same solution:

$$\omega_{1,2} = \sqrt{\frac{(L_1 C_1 + L_2 C_2) \pm \sqrt{(L_1 C_1 - L_2 C_2)^2 + 4 L_1 L_2 C_m^2}}{2(L_1 L_2 C_1 C_2 - L_1 L_2 C_m^2)}} \quad (2.10)$$

If we have $\omega_{01} = (L_1 C_1)^{1/2}$ and $\omega_{02} = (L_2 C_2)^{1/2}$, then the coupling coefficients are

$$\begin{aligned}
K_e &= \frac{C_m}{\sqrt{C_1 C_2}}, K_m = \frac{L_m}{\sqrt{L_1 L_2}} \\
&= \pm \frac{1}{2} \left(\frac{\omega_{02}}{\omega_{01}} + \frac{\omega_{01}}{\omega_{02}} \right) \sqrt{\left(\frac{\omega_2^2 - \omega_1^2}{\omega_2^2 + \omega_1^2} \right)^2 - \left(\frac{\omega_{02}^2 - \omega_{01}^2}{\omega_{02}^2 + \omega_{01}^2} \right)^2} \quad (2.11)
\end{aligned}$$

In our case and many other applications, resonator coupling may use both electric and magnetic coupling. This model can still be used to derive a universal expression for coupling when both coupling mechanisms are present. Equation 2.11 is still valid for this combined case. Although the derivation is done in a lumped element model, the coupling coefficient also works for distribution parameter systems, such as microstrip transmission lines. The expression in equation 2.11 is different from equation 2.2 because equation 2.2 is particular to the coupled mode theory. What is important for determining energy distribution in a multiple-resonator system is the relative ratio of those coupling coefficients given in equation 2.2, instead of their absolute values. In other words, two set of coupling coefficients with the same relative ratio but different absolute values would produce the same energy distribution according to CMT. On the contrary, equation 2.11 represents its absolute value and is appropriate for two resonator systems such as microwave filter and coupler designs.

To conclude, the power sharing theory among multiple coupled resonators called coupled mode theory has been analyzed specifically for linear and circular plasma arrays. CMT results in multiple resonances and thus multiple modes for the plasma to operate in. However, there is only one desired mode to generate uniform plasma for the linear array and only two modes for the circular array. In order to balance the considerable center-to-edge power difference of the linear array in the 1st mode, a direct coupling strip has been introduced to ameliorate the weak coupling to edge resonators. The effect of parasitic plasma impedance has been modeled and estimated for the circular array to illustrate a particular plasma instability. Higher modes operation has also been discussed to complete the understanding of CMT. Finally, the derivation of the critical CMT parameter, the coupling coefficients, has been carried out based on the lumped LC model. In the following section, linear and circular arrays will be modeled

using a high frequency electromagnetic simulator to illustrate the spectral behavior and electric field distribution among the resonators. It will be confirmed that the previous analysis of CMT and direct coupling strip are valid and reasonably accurate models.

3 Simulation results

In addition to coupled mode theory for the linear and circular arrays, simulation is still necessary in order to find system input impedance and get a measure of the uniformity of electric field distribution before building the arrays and performing the experiments. In addition, if all the parameters are meticulously defined in accordance with real experimental array structures, impedance matching tuning could be mostly done in this step to ensure deep resonance and maximum power delivery. The circular array simulation results will be presented first before the effect of direct coupling strip on the electric field uniformity of the linear array is demonstrated. Higher operation modes derived from CMT will also be verified from simulation outcomes. Finally, magnetic and electric coupling mechanisms will be explained.

3.2 Circular array

The simulation results for the circular array are basically S-parameter and electric field strength and uniformity illustration. Since no direct coupling strip is necessary for the intrinsic uniform electric field distribution at the 1st mode, simulation for the circular array is fairly simple and straightforward.

3.1.1 S-parameter of the circular array

The S-parameter of the circular array is shown in figure 3.1 where the simulation curve is the reflection coefficient S_{11} as a result of using Ansoft Corporation's High Frequency Structure Simulator (HFSS) to solve the Maxwell's equations for the 3-D structure. After analyzing the electromagnetic field through this finite element method of using a large number of meshes (typically 100,000 to 250,000), the solver outputs the reflection coefficient with respect to frequency. Each reflection coefficient minimum denotes a resonance frequency where power is absorbed by the array. According to CMT, we would expect six resonant frequencies, but as stated before two pairs of these resonances are degenerate and cannot be resolved due to two overlapping resonances. This is even more pronounced for the experimental measurement curve where the 3rd mode is broadened as compared to the normal single mode, indicating that there could

be two resonant frequencies that are too closely overlapping with each other and appear as one resonance.

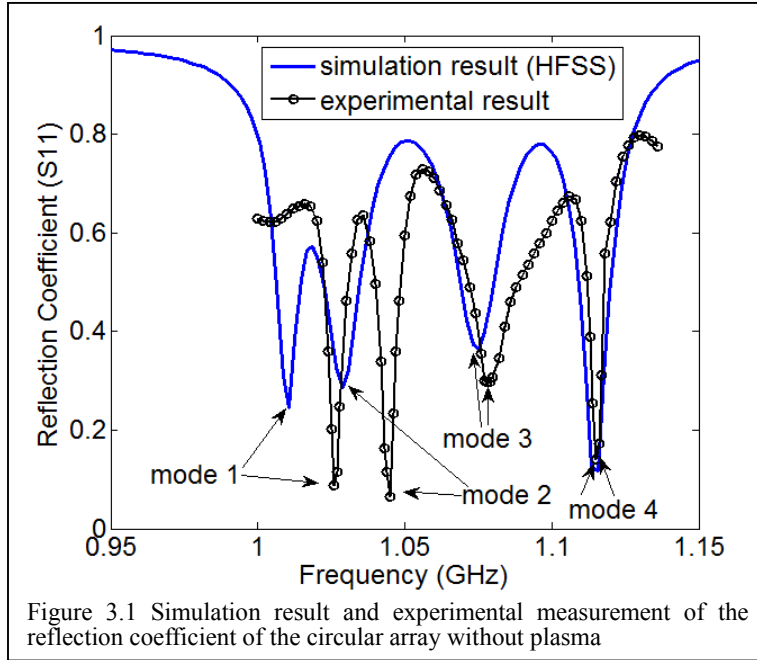
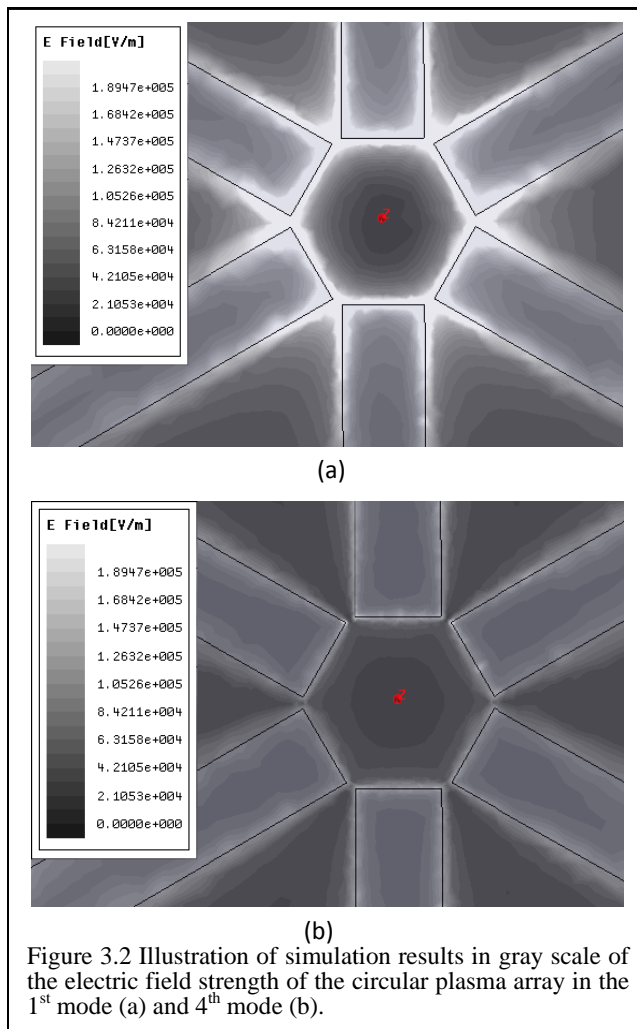


Figure 3.1 Simulation result and experimental measurement of the reflection coefficient of the circular array without plasma

3.1.2 E-field and higher modes discussion for the circular array

The electric field magnitude corresponding to the resonant frequencies of mode 1 and 4 is illustrated in figure 3.2 (a) and (b) since these two modes are desired for their abilities to generate uniform plasma due to their uniform electric field distribution. The electric field distribution at the first mode is in agreement with CMT solution. With the same scale as the first mode, electric field in the fourth mode (figure 3.2(b)) is significantly weaker with the same amount of input power. Another substantial difference is that in the first mode, the electric field is mainly from a resonator tip to its two neighboring resonator tips; while the field in the fourth mode mainly resides on its own tip and there is a minimum in the 0.1mm gap from one tip to its neighboring resonator tips. This implies that the 1st mode electric field is uniform among all the resonators, but 4th mode is uniform on individual resonator and there will be insufficient electric field in between any two resonators to generate plasma. Thus, albeit the 4th mode power distribution may be uniform as far as CMT is concerned, the real electric field configuration could be entirely different. Not all the electric field configurations are

suitable for generating the uniform plasma in a ring-shape as we desire. As will be shown in the next section, the electric field of the first mode forms a ring-shape plasma but fourth mode electric field causes plasma to be on each resonator and then extends from the resonator tips to the center of the array. From this result, we find that the simulation of the electric field gives a fairly good prediction of the plasma shape, with the caveat that the simulation does not account for any parasitic plasma effects. Therefore, the first mode is preferred in generating uniform plasma in terms of electric field strength and its location with respect to the resonator tips.



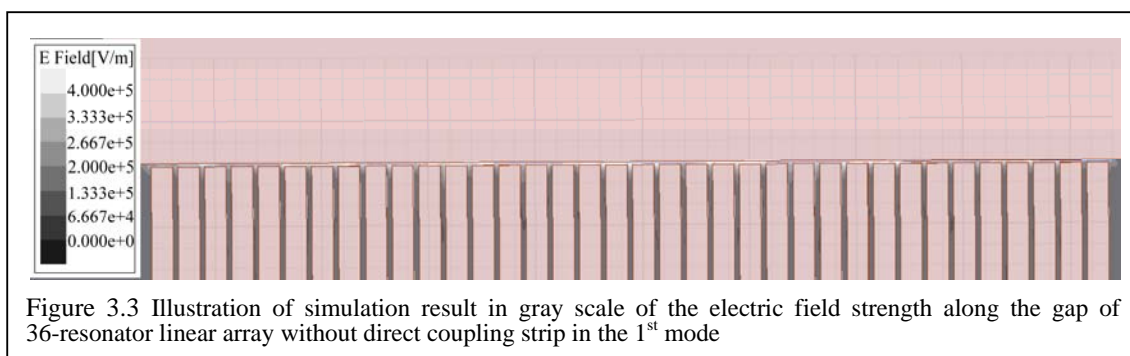
3.2 Linear array

One distinction of the linear array from the circular array is that linear array can be scaled-up and extended as long as uniform plasma could be generated. Hence, before

the 72-resonator linear array was designed and fabricated, attempts have been made for shorter arrays starting from 5 resonators [22]. Without the direct coupling strip, independent resonators could only sustain uniform plasma on a limited number of resonators due to the previously described plasma instability and a lack of power delivered to the edges of the array. So, in the simulation analysis of the linear array, 36-resonator arrays with and without the direct coupling strip will be compared for electric field uniformity. The higher modes operation will be demonstrated and discussed using a 72-resonator array for the reason that the longer array has more modes with discernable resonances in the spectrum. So, the S-parameter profile will be illustrated as well as the corresponding higher modes electric field distributions.

3.2.1 E-field and S-parameter without DCS

Linear plasma arrays composed of 5 and 16 elements have previously been attempted both in simulation and experiment [25]. In this work, an array of 36 has been simulated to gain a knowledge of the electric field configuration. Several adjustments have been made to the structures of the previous arrays, namely the spacing between microstrip lines has been shrunk to 0.25mm, which is about one-quarter of the resonator width, in order to enhance power coupling; the gap from the each resonator to the ground plane has also diminished to a gap of 0.15mm to maximize the electric field in the gap for a given voltage at the resonator tip.

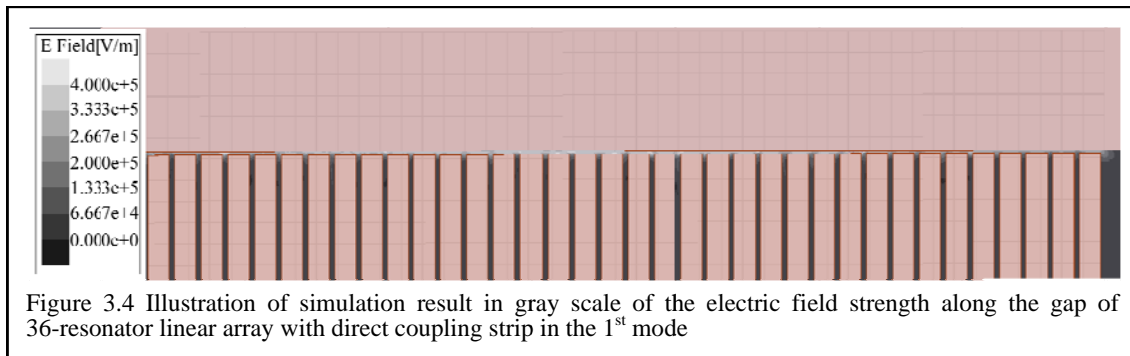


For the 36-resonator array without a direct coupling strip, figure 3.3 shows the HFSS simulation snapshot of the electric field magnitude in the gap in color scale. In this case, the input power is delivered via the 18th resonator from the left. The question as to the

choice of input power position will be discussed in section 3.2.3 as this affects operation of higher modes which may play some important role when superposition of modes is necessary. The center portion is mostly red indicating very strong electric field exists there ($E \sim 4 \times 10^5$ V/m at 1 watt), while the region near the edges is green to blue meaning much less field strength. Since simulations that include indirect electric and magnetic coupling show that coupling is not strong enough to induce uniform electric field on all resonators, it is not surprising that the resonators in the center area experience stronger electric field than edge resonators. To get a quantitative idea of the field strength variation, a plot will be given in the following section in terms of the electric field strength along the horizontal length of the discharge gap. In the same plot, the electric field strength of the same length array structure including a direct coupling strip will be compared with respect to field uniformity.

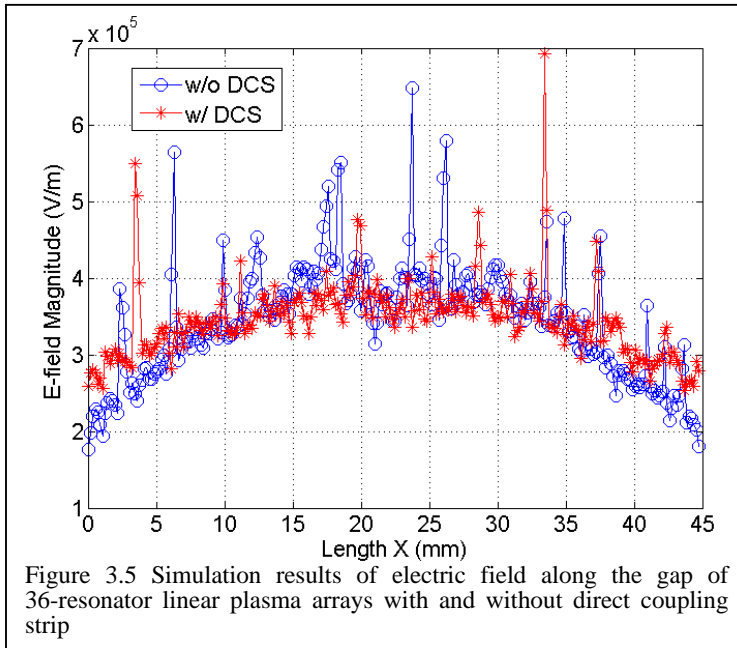
3.2.2 E-field with DCS

In this section, HFSS is used to examine the electric field uniformity when a direct coupling strip (DCS) is used. Similar to figure 1.2, this linear 36-resonator array simulation has 36 resonators in parallel and has a direct coupling strip across the input connector pin connecting all of the resonators. In the theory section, the DCS has been shown to alleviate the issue of center-to-edge electric field non-uniformity, but CMT cannot predict to what degree the DCS will help. Hence, the simulation was performed and the result in the figure 3.4 shows the electric field magnitude in the gap.



From the picture with same scale as in figure 3.3, there is no large red area at the center, but almost all yellow indicating a more uniform field exists in the discharge gap region.

The input power is distributed toward the edge resonators reducing the peak electric field in the center of the array. The electric field along the gap can be plotted against length as is shown in figure 3.5 where a comparison of the effect of the direct coupling strip on field distribution is done. The DCS simulation data was normalized to match the field strength in the central region of the array for easier comparison. Given the same amount of input power, the total power should be the same in two scenarios meaning that the square of the integrated area below the curve should coincide. So, in the original case, the concentration of the input power is located on the center resonators and most electric field is also in this region; while the latter case distributes the power more uniformly among the resonators and this may eventually help generate a more uniform linear-plasma.



Because of the improvement brought by the new DCS scheme, efforts have been spent on some other innovative methods in order to reinforce the power coupling among the resonators and directly deliver power to the edge resonators, such as two or multiple direct coupling strips; different strip widths; different strip positions with respect to the input node, and even an additional layer of the coupling strip above the plane of the array. However, no significant benefit has been witnessed in simulations as a result from these new designs. Thus, only the above two device configurations were built and

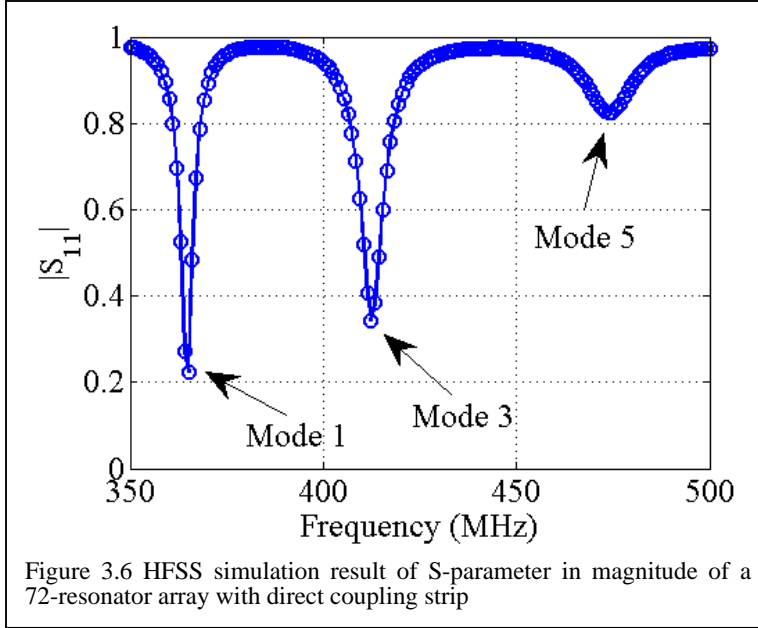
tested in the experiments, and these will be compared and discussed in the section 4.

3.2.3 E-field and current patterns of higher modes

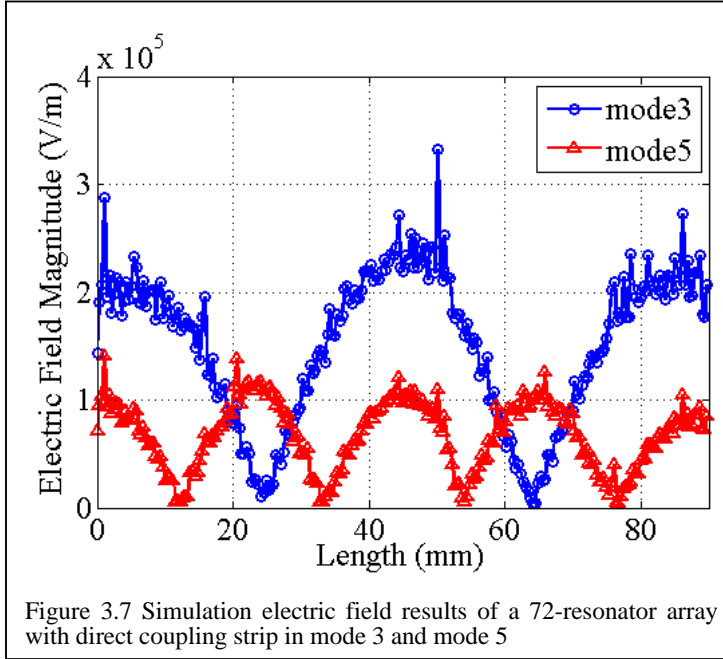
Since the longest array ever tried at this frequency range in the experiment is the 72-resonator array, which is about 90mm long, the simulation of this array is used to demonstrate the higher modes and their electric field and current patterns.

As shown in figure 2.8, and mentioned above, the higher the operating mode is, the more the number of the spatial power maxima will be. For instance, in mode 1 there is one power maximum at the center and it tails down towards the edges; in mode 2 there are two power maxima and the edges still have the minimum power thus there has to be a power minima at the center; in mode 3 there are three power maxima and the two edges are always minimum power. So, if we follow this logic at the n^{th} mode there are n power maxima and edges still experience the lowest power. This is part of the reason why a single higher mode is not suitable for generating uniform plasma. In general, only a couple of resonant frequencies may be conspicuous on the spectrum and all higher degenerate modes are submerged either due to poor impedance matching at that resonant frequency or the suppression resulting from the input power position. Specifically, for example, in the 2^{nd} mode the power distribution sees a minimum at the center. If power is input to the array at the center resonators, the power will not be absorbed by the array in any even mode and thus it acts like there was no resonance at that frequency. So, in the previous section dealing with the 36-resonator array simulation as well as the present 72-resonator case, the input power is at the center for both situations. Doing this causes the 2^{nd} mode and all the rest even number modes to be suppressed as illustrated in figure 3.6 below which shows the reflection coefficient magnitude($|S_{11}|$) against frequency for the 72-resonator linear array with direct coupling strip. Thus, if we wish to operate a plasma using a superposition of the 1^{st} and 2^{nd} mode, it cannot be done if the input is located at the center. But the feasibility of a combination of 1^{st} and 3^{rd} mode is not affected. The reason for the center-input choice is to exert no bias on either the left or right side of the array. As will be reported,

experimental testing suggests that the 1st mode alone is usually enough to generate uniform plasma at the given array length, so usually there is no need for superposition of higher modes to control uniformity.



The addition of the direct coupling strip does not change the mode caused by input port location because it does not have much effect on the power distribution at the center but just helps to deliver power to the edges. However, DCS does make some differences in the reflection coefficient profile and the edge electric field strength. Specifically, the spacing between two resonant frequencies in figure 3.6 is relatively constant while in the case without the direct coupling strip, the higher modes tend to squeeze together and overlap with each other and eventually they become degenerate. As a demonstration of the field patterns created by higher modes, the electric field magnitude along the gap in the 3rd mode and 5th mode of the array with DSC is plotted in figure 3.7. In contrast to the CMT prediction for independent resonators, edge resonators always experience local minima for the electric field magnitude, the DCS causes higher modes to have fairly large electric field at the edges array, even if they are not strictly at maxima.



In the CMT model, the power distribution was plotted in terms of the absolute value of $a_m(t)$ which did not reveal the phase information of the electric field. In fact, the phase profile can be best represented by the surface current vector on the array. As figure 3.8 (a) illustrates, the first mode has the current on all the resonators in the same direction (phase) indicating that the electric fields at all of the tips are in phase (although there may be a little phase delay from the input resonator at the center to the edge ones). Although the 2nd mode is suppressed in this array, if there were a 2nd mode it would divide the current pattern into two parts. Current on the right portion of the array would be 180 degrees out of phase with the left portion. Effectively, the current would flow from left part of the array through the direct coupling strip to the right part. Therefore, the electric field of the right and left halves is in the opposite direction. Actually, this 2nd mode hypothesis has been verified by simulating arrays with the input power port not being at the center resonator position. In the 3rd mode illustrated in figure 3.8 (b), the center portion is out of phase with both edge portions which are in phase. And the current pattern is from the edge resonators going through the direct coupling strip to the center ones. Therefore, the electric field follows the phase profile that center field is out of phase with edge fields. Following the logic, in the 5th mode as shown in figure 3.8 (c), the array is divided into five portions and every other portion is in phase and two

neighboring portions are out of phase. These phase observations from the HFSS simulations are also predicted by CMT. The direct coupling strip provides a conduction path between two neighbor portions. So, surface current is strong and pronounced along the horizontal strip in the figures.

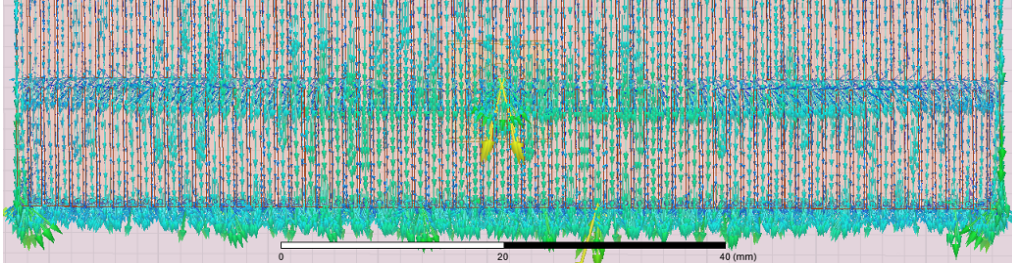


Figure 3.8 (a) Simulation result of surface current at 1st mode of 72-resonator array

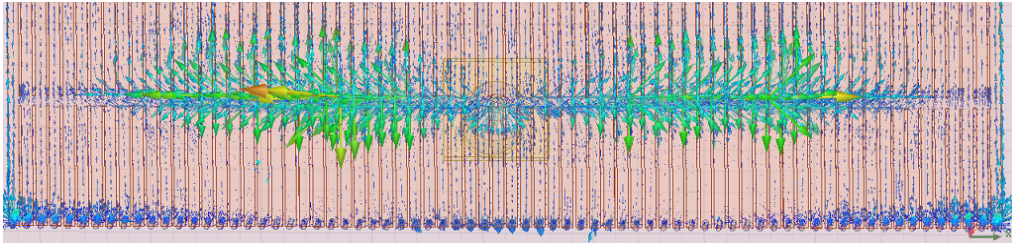


Figure 3.8 (b) Simulation result of surface current at 3rd mode of 72-resonator array

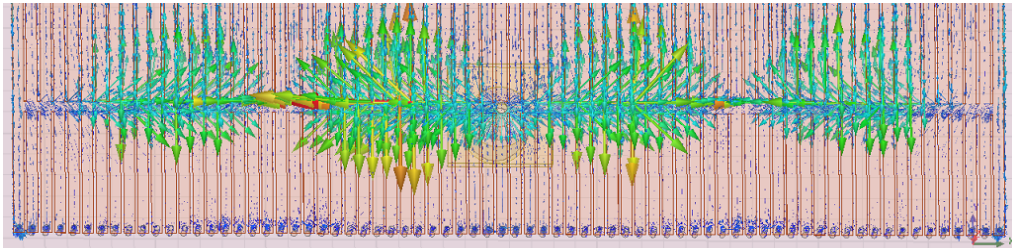


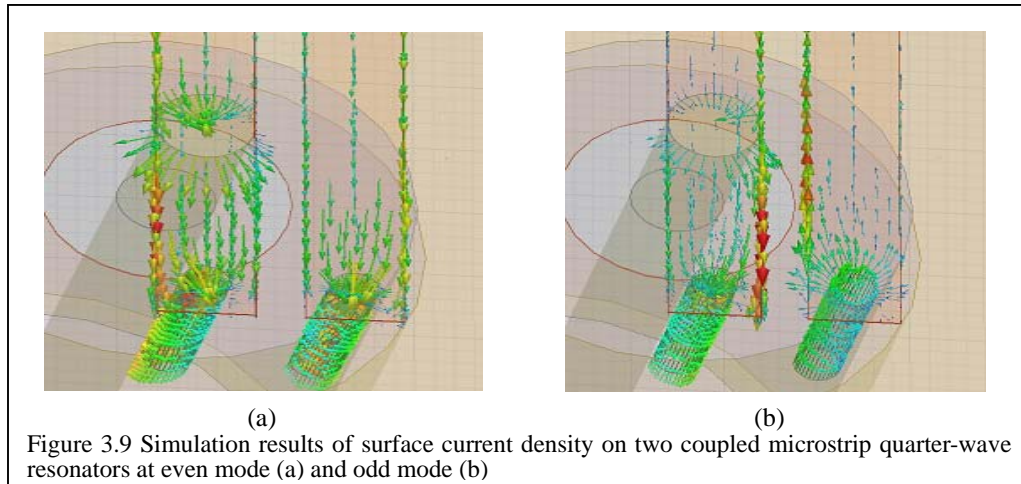
Figure 3.8 (c) Simulation result of surface current at 5th mode of 72-resonator array

Before we show the experimental arrays in argon plasma, the coupling resulting from mutual fields can also be demonstrated using the electromagnetic simulator. So, we will give a brief idea of the electric and magnetic mutual fields between only two resonators in parallel with no direct conduction path, which is the simplest scenario for analyzing the coupling mechanism.

3.3 Magnetic and electric coupling demonstration

The coupling between two microstrip lines is believed to be from the mutual and interacting electric and magnetic fields. In the section 2.1.4, the mutual electric field is

modeled as a lumped capacitor and magnetic field as an inductor. For this discussion, we take two parallel microstrip lines as an example and define the even mode as the mode in which the surface currents are in phase and the odd mode out of phase as shown in figure 3.9. Therefore, the voltage at the input point of each resonator satisfies $V_1 = V_2$ in the even mode and $V_1 = -V_2$ in the odd mode. Any input to these two resonators can be modeled as a linear combination of the even mode and odd mode. So, in our case we have $V_1 = \frac{V_{in}}{2}, V_2 = \frac{V_{in}}{2}$ for the even mode and $V_1 = \frac{V_{in}}{2}, V_2 = -\frac{V_{in}}{2}$ for odd mode. Considering the addition of these two modes, we get $V_1 = V_{in}, V_2 = 0$ since we are only supplying power to one resonator. In both cases, these two coupling mechanisms are taking place. In more detail, in the even mode as shown in figure 3.10(a), although the collective effect of the electric field at the tips are parallel with each other going from the conductor to the ground, the individual fringing electric field from each resonator is believed to go to the other resonator inducing charges and thus coupling energy. In figure 3.11(a), the cross section in parallel with and in between the resonators is perpendicularly crossed by mutual magnetic fields resulting from the two via currents which is also a means of transferring energy. In the odd mode, it is straightforward that electric field goes from one resonator to the other due to the fact that the fields are out of phase as illustrated in figure 3.10(b), while the magnetic fields parallel with the cross section are interacting in figure 3.11(b) because there is a mutual region where magnetic fields from two resonators are present and co-directional. These two mutual fields give rise to the energy coupling in both cases.



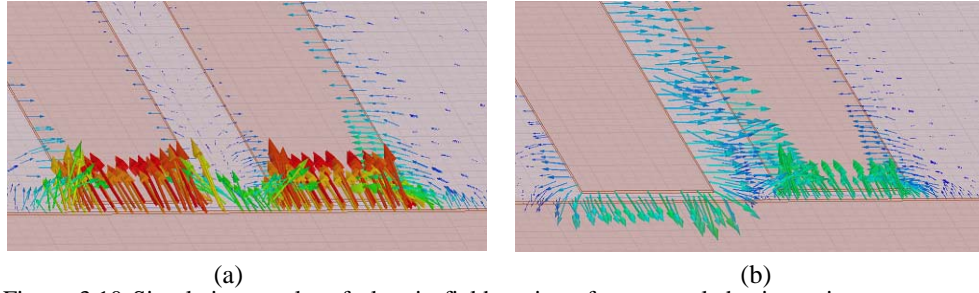


Figure 3.10 Simulation results of electric field at tips of two coupled microstrip quarter-wave resonators at even mode (a) and odd mode (b)

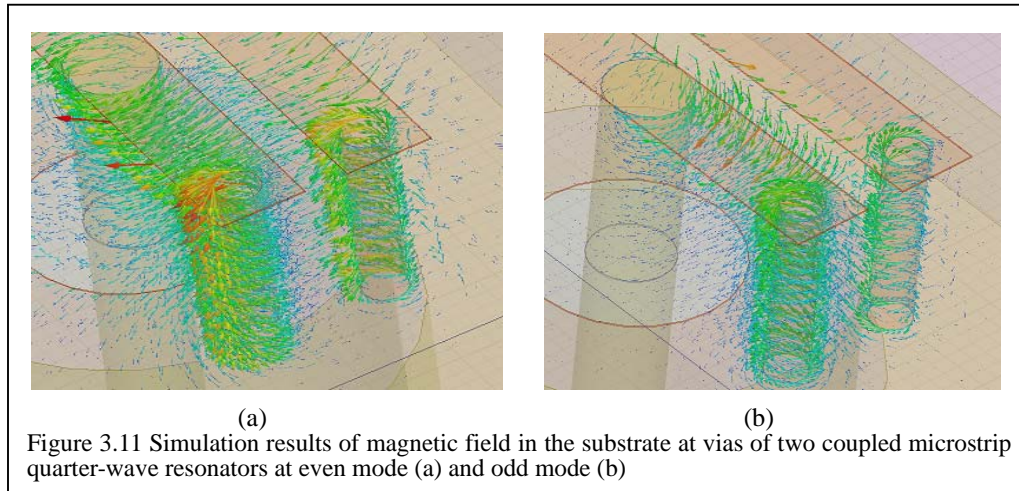


Figure 3.11 Simulation results of magnetic field in the substrate at vias of two coupled microstrip quarter-wave resonators at even mode (a) and odd mode (b)

In summary, this section 3 describes a simulation interpretation of the theory given in section 2. It has been verified so far that the simulation results agree with the theory prediction. That is to say the supporting theory is a correct and useful model. However, when we included the parasitic plasma effects this resulted in unbalanced electric fields and might even cause instability due to expanding plasma capacitance. So, we will show next the plasma formed by the circular array and the linear array that were just shown in simulations. As anticipated, arrays with only indirect coupling result in a non-uniform distribution. Nevertheless, this parasitic plasma capacitance effect can be reduced by using dielectric limiters. It will also be shown that the direct coupling strip is sufficient to sustain uniform plasma along the length of the gap, even without the dielectric limiters.

4 Experimental results

First, the experimental setup and procedure will be briefly introduced. We will discuss the circular array first. The 1st and 4th circular modes which have been showed by CMT to form uniform electric fields, will be demonstrated first. Then, we will demonstrate that uniform plasma can be generated with the help of dielectric limiters and the uniformity of the array will be quantified by measuring the spatial emission intensity of the plasma. The same analysis will be applied for linear array of 36-resonator both with and without a direct coupling strip. These two cases will be contrasted. The advantage gained by the direct coupling strip will be utilized to build the 72-resonator array and the emission intensity will also be shown to verify the plasma uniformity.

4.1 Experimental setup and procedure

An LPKF micro-milling machine is used to fabricate the 6-resonator circular array and the various linear arrays on RT/Duroid 6010.2 copper laminate. This is a microwave circuit board material with relative dielectric constant of 10.2 and is plated with 17.3 μ m thick copper on both sides. One side of the copper is used as a ground plane for the devices and the other side is milled with the array pattern. Input power signal is delivered through a subminiature type-A (SMA) connector mounted through a tapered port on the side of the circular array which is known as side-port means. The input taper is placed to ensure best impedance matching and maximum power delivery. For the linear arrays, the input port is soldered from the ground side of the arrays and this is known as under port means. The input pin is 12mm away from the short-circuited end of the linear array so as to also match the SMA's 50ohm characteristic impedance. The signal generator and power amplifier are an HP 8656A and ENI 525LA respectively. An HP 438A power meter and HP 8481A power sensors are used to find the forward and reflected power as well as the reflection coefficient (S_{11}) of the array simply by taking the ratio of the reflected to the forward power.

To generate plasma in argon, the arrays are placed inside a chamber and all air is evacuated by a mechanical pump with base pressure of ~2 Pa before argon is backfilled

until atmospheric pressure is reached (750Torr). An MKS piezoelectric transducer (P/N 100 012 621) and a Granville-Phillips 275 Convectron Gauge with a precision of 1Torr (133Pa) and 1mTorr (0.133Pa) respectively are used to measure the pressure inside the chamber.

4.2 Circular array

4.2.1 Side port 1st and 4th modes

The plasma generated using the circular array at the 1st mode and 4th mode is presented in figure 4.1 and figure 4.2. In both pictures the input power is delivered to the bottom resonator in the photograph. The plasma in the first mode exhibits the similar behavior as given by the electric field in the HFSS simulation in figure 3.1. Recall that the electric field is mainly between every two resonator tips in the 1st mode and this is where plasma is observed to form. There are still three small tip regions on the resonator 3, 4 and 5 that are not completely covered by plasma. In addition to this non-uniformity, the plasma extends a little beyond the tip on the bottom resonator. This is because of the resonant frequency downshifting due to the plasma sheath capacitance causing more power to go to the resonator according to CMT as illustrated in figure 2.6.

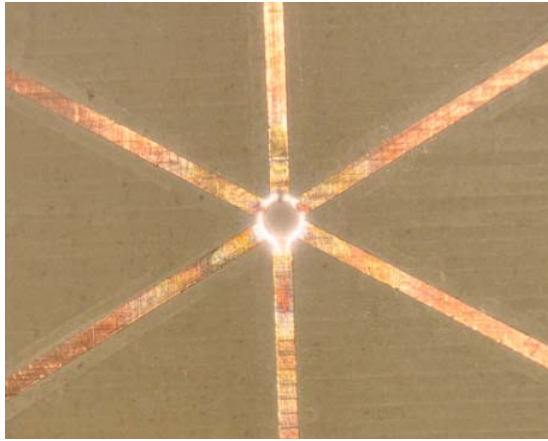
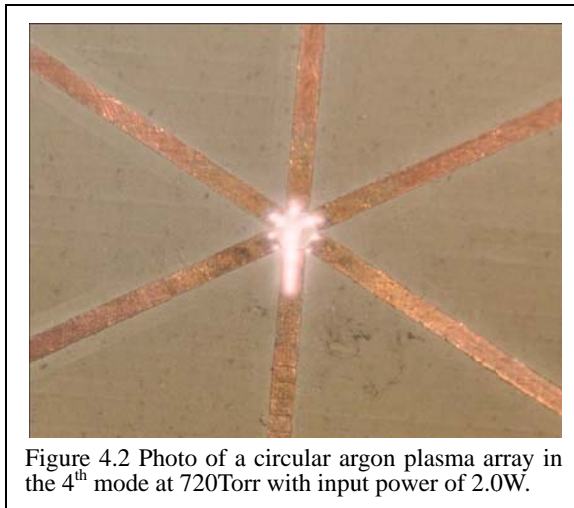


Figure 4.1 Photo of a circular argon plasma array in the 1st mode at 720Torr with input power of 1.8W.

In the contrast to the 1st mode, but as expected, the plasma forms from each resonator toward the center (rather than between tips) in the 4th mode as seen in figure 4.2. This observation is also consistent with what was predicted by the simulated electric field in

figure 3.2. In this case, the plasma on the bottom resonator extends beyond the tip much more than the first mode resulting in asymmetry of the CMT-predicted eigenvector and the actual plasma power distribution. Since there is a strong current going from the bottom resonator to the plasma due to the asymmetry, a large plasma sheath area is needed to conduct that amount of current. Although not shown here, modes 2 and 3 are basically combinations of mode 1 and mode 4 with plasma forming a circle along the six tips as well as from the electrode tips to the center. These two modes are considered intrinsically less desirable due to inherent non-uniformity.



4.2.2 Improving uniformity with dielectric limiters

It has been anticipated that operating the array in the first mode would form uniform circular plasma. However, due to the non-uniformity of plasma expanding beyond the tips and three spots absent of plasma, the uniform power distribution is disturbed by the plasma's capacitive and resistive nature. So, to prevent this asymmetric disturbance, plasma must be confined in a ring-shaped region where only limited microstrip tip area is exposed to the plasma. As shown in figure 4.3, the dielectric material Duroid has been used to build the 1 mm thick plasma limiter which is composed of two pieces, the outer ring with o.d.=10mm and i.d.=2.5mm and central dielectric cap of 2mm diameter. This set of plasma limiters covers most of the tip area where the extra disturbing plasma capacitance is usually located and only exposes the same amount of area for each resonator to sustain plasma. Figure 4.3 shows the plasma generated with

the limiter covers attached with total power of 2.5watts at 0.99GHz. The inserted photograph was taken without any photoflash and a smaller f-stop to ensure that no pixel is saturated. Taking the photograph without illumination has another benefit of demonstrating that no parasitic plasma penetrates under the translucent dielectric limiter. Thus, a circular microplasma is generated at atmospheric pressure with the help of dielectric limiters to prevent asymmetric frequency shifts due to unwanted plasma sheath capacitance.

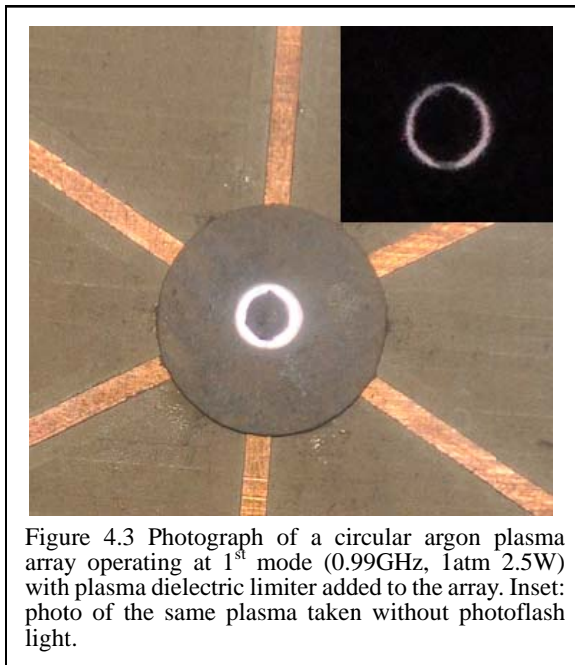
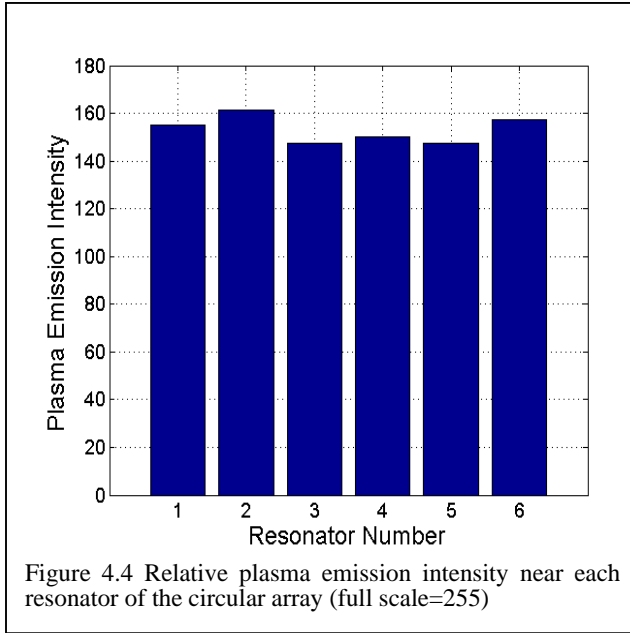


Figure 4.4 plots the plasma emission intensity from each resonator based on the inset photo in figure 4.3. Every color pixel is first converted to gray scale (0-255) and then pixels that exceed the noise threshold (50) were summed over a 1.0mm width near the resonator tips and finally the sum was divided by the total number of non-noise pixels. Every pixel that is less intensive than the noise threshold value is set to zero with those more than the threshold unaffected to simplify the calculation. The threshold value is set in such a manner that the recorded mission intensity far from the circular plasma is below the threshold and much less than being comparable to the plasma intensity within the array. From the figure, the emission intensity shows reasonable uniformity with a slight maximum at the 2nd resonator and a minimum at the 3rd resonator. This demonstrates that the symmetric nature of the coupling coefficient matrix in CMT for a

circular array is capable of generating a uniform microplasma array. The tendency of microplasma sheath capacitances to unbalance the even distribution of power among the elements of the array can be overcome by the resonator tips with a 1 mm thick dielectric limiter.



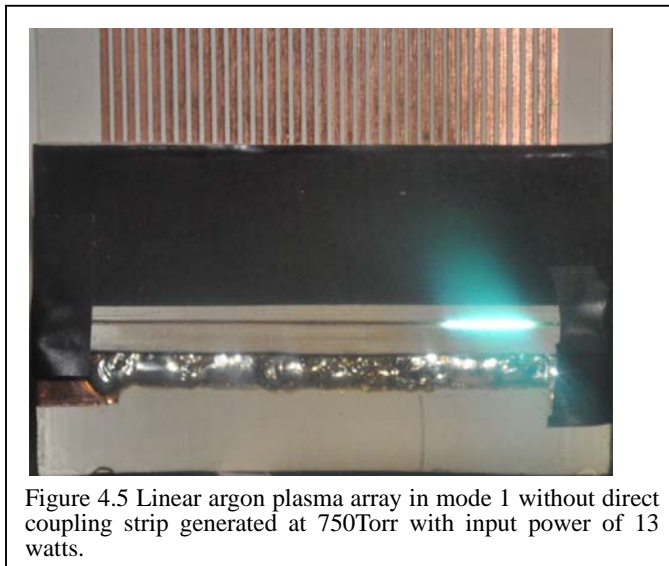
4.3 Linear array

An intermediate step of 60-resonator array has been attempted before the 72-resonator array with the same overall effect in terms of stability, uniformity and emission intensity. Thus, its description will be omitted here. Although dielectric limiters have been used for the 36-resonator linear arrays, it will be shown that the direct coupling strip helps a linear array to generate plasma on all resonators in a fairly uniform fashion even without the dielectric limiters. Emission intensity along the gap will also be measured and plotted to quantify the uniformity of the microplasma.

4.3.1 First mode uniform plasma with dielectric limiters

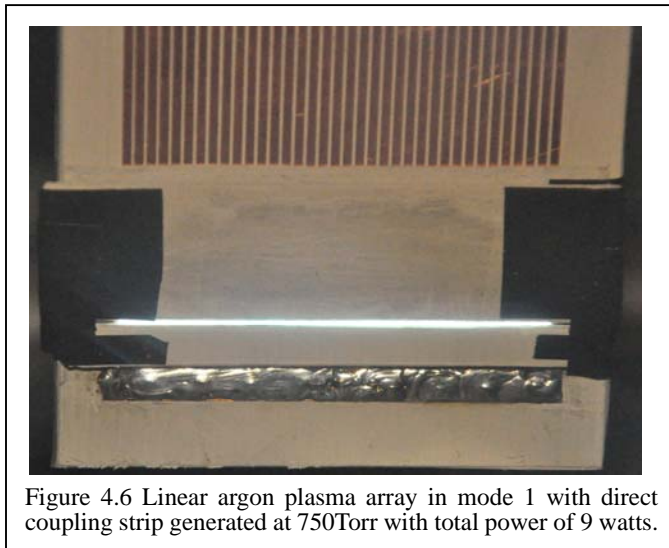
The linear 36-resonator array simulation shown in figure 3.3 and 3.4 demonstrated the benefit of the direct coupling strip in increasing plasma uniformity. Figure 4.5 and 4.6 are presented here to show the actual plasma array without and with a direct coupling strip, respectively. As the dielectric limiter has done a good job restricting the plasma for the circular array, the same idea is also applied to the linear plasma. This limiter was

attached using the black insulating electric tape in the figures. Figure 4.5 shows the plasma array in mode 1 without DCS at 750Torr with 13w total power. The power input port is located at the 9th resonator from the right. The reason for placing it at this particular position is to allow the possibility for 1st, 2nd and 3rd mode superposition but the application of power to the 9th resonator blocks the 4th mode. Simulation has already shown strong resonance of the lower modes because of good impedance matching. If the input was placed at any other position so that 4th and higher mode can be used, they would possibly be too reflective to be useful.



From figure 4.5, even at pressures lower than one atmosphere not all the resonator could generate plasma at their tips. Moreover, a brighter plasma is easily observed at region about the tip corresponding to the input resonator (#9 from the right) indicating that more power is going to that plasma location. This is highly undesired because this may cause the transition from cold plasma to a hot arc which is destructive and will damage the array. As a result, in the presence of plasma effect weak coupling among adjacent resonators alone is not enough to handle the uniform power distribution task. Plasma is initially ignited at the input resonator tip and then changes the resonant frequency of that resonator by loading it with the plasma capacitive sheath. This leads to more power going to that resonator as predicted by CMT. Without any method to prevent this positive feedback effect, it will ultimately result in a transition to a plasma arc well before the power is sufficient to fully ignite plasma across the array.

On the contrary, the DCS does a good job spreading the power more evenly among the resonators which can be verified in figure 4.6 where plasma is sustained in the first mode at 750Torr with total power of 9watts. In this particular device, the input port is also located on the 9th resonator from the right. Plasma is present on all the resonator tips at atmospheric pressure with less power consumption than experimental array without a DCS. Thus, the arc transition instability is substantially ameliorated. With the success of DCS, the concept looks promising to extend to a longer linear array.



The longest array attempted so far is the 72-resonator system. The 72-element array is 90-mm long and is sustained by an input power of 20.9watts in argon at 750Torr as shown in figure 4.7. The plasma is operating in the first mode at 366MHz in the upper subfigure without dielectric limiter covers. Even without limiters, though the linear plasma array could have plasma on all the resonators ignited, but there is some obvious non-uniformity in terms of plasma's vertical extent along the microstrip. Specifically, plasma tends to grow bigger at the areas close to but not right on the edges. This phenomenon is possibly particular to argon since no such problem has been observed in helium gas. The bottom photograph shows the array operating in argon with limiters. This photograph was made without a flash so that the uniformity of plasma emission intensity could be measured. The addition of dielectric limiters on both the tips and the ground causes the first mode resonant frequency to slightly change to 360MHz. Again, there is no parasitic plasma under the limiters and the snapshot has been taken with

1/4000 shutter speed and an $f=5.6$ aperture number to ensure no pixel saturation.

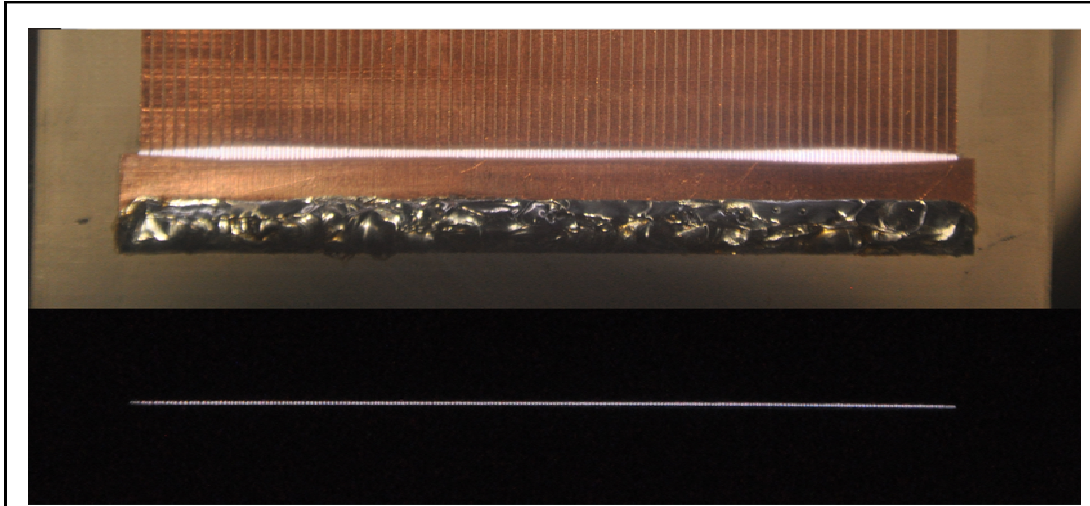


Figure 4.7. Photograph of experimental 72-element linear plasma array in argon at 750Torr (1 atm) with input power of 20.9 Watts in the 1st mode.

The emission intensity of the lower subfigure of figure 4.7 is plotted in figure 4.8. Each blue intensity bar is the average pixel value in gray scale (0-255) of a 35-pixel wide column after excluding the noise pixels whose values are less than the threshold value which is set in the same fashion as the one in the circular array. The noise pixel values are set to zero to simplify calculation and they are not counted as valid pixels when doing the averaging. From the figure, the intensity is fairly uniform especially at the center with some slight tailing off at the two edges.

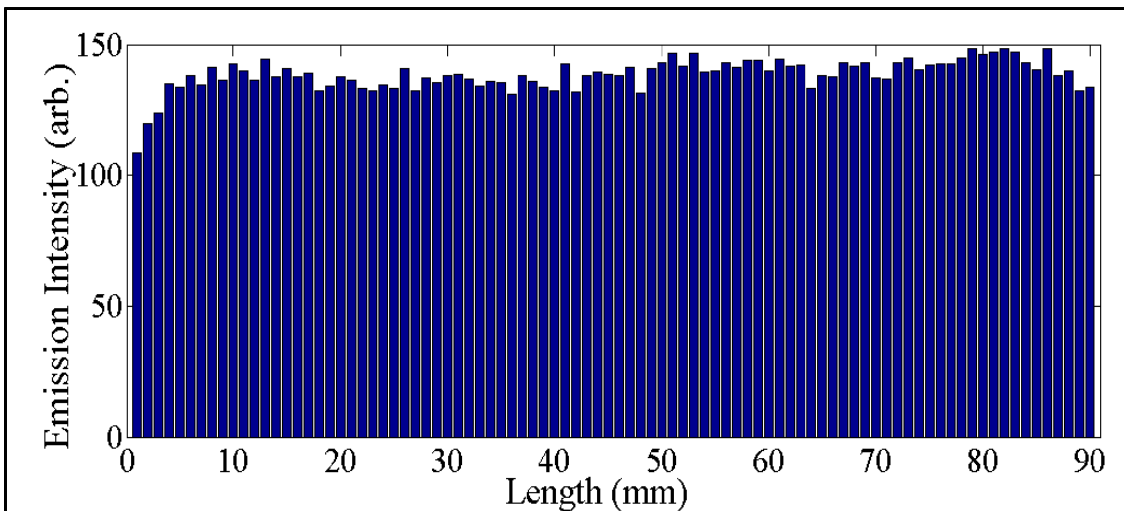


Figure 4.8 Emission intensity of the 90mm linear argon plasma array with dielectric limiters as shown in the lower part of figure 4.7.

4.3.2 Higher modes in comparison with simulations

In consistency with section 3.2.4, the experimental result of 3rd and 5th mode of the 72-resonator linear array with DCS and dielectric limiters is shown in figure 4.9. It may not be clear from the figure since there is no flash light, but the edge resonators are all ignited which agrees with the simulation results shown in figure 3.7. Since the input connector is located at the center of the array, the 2nd, 4th and higher even number modes are suppressed due to the CMT-predicted power minimum at the center of the array. These results are of scientific interest, but the first mode is preferred to generate uniform plasma. The 3rd or other higher mode alone is not sufficient to obtain uniform plasma. However, superposition of 1st mode and 3rd or 5th mode is feasible to have uniform plasma, but no significant uniformity benefit has yet been observed.

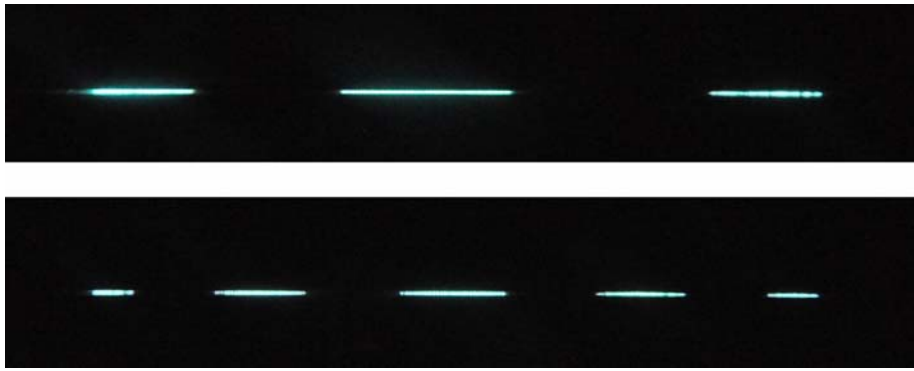


Figure 4.9 Photo of experimental argon plasma in 3rd and 5th mode at 750Torr (1atm) with dielectric cap limiters.

5 Conclusion and future work

5.1 Uniform plasma arrays with RF sources at atmospheric pressure

Atmospheric argon plasma has been demonstrated to operate uniformly in a circular and linear fashion by means of coupled resonators. Starting from the straightforward idea of a quarter-wave microstrip line resonator to provide large electric field to facilitate the plasma ignition at atmospheric pressure, two typical assemblies of multiple resonators have been studied and experimentally tested. Coupled mode theory has been analyzed and presented in matrix form, and homogeneous and particular solutions have been found to show the power distribution without plasma for these two arrays. In particular, the linear array has gone through major modification of an additional direct coupling strip to ameliorate the inherent drawback predicted by coupled mode theory due to the single-sided weak coupling at the array edges. After theoretical and simulation verifications, both circular arrays and linear arrays have been shown to be able to form uniform argon plasma, especially with the help of dielectric limiters that limit undesired parasitic plasma. Higher mode phenomena resulting from coupled mode theory have also been illustrated in simulations and experiments.

Because of their small sizes, low power consumption and operation at atmospheric pressure in the absence of any vacuum pump, these arrays can be implemented in portable devices. For the circular array in applications, the center region which is covered by the limiter would be drilled out to allow materials, liquids and gases to be continuously treated by the surrounding plasma. For the linear array, roll-to-roll coating can be easily implemented with the sheet to be processed continuously moving above the plasma line. If the sheet is some reasonable distance away from the plasma, the plasma seen by the sheet will be more uniform than the experimental intensity plot since the plasma filaments will be blurred by diffusion.

5.2 Future work

5.2.1 Higher frequency operation

Although both arrays have been successfully designed to operate in the radio frequency and UHF range, higher frequency operation will be sought such as microwave

frequency range. For example, desirable frequencies include the cell phone communication frequency bands between 850 MHz and 1900 MHz or even higher at the typical microwave oven frequency of 2.45 GHz. Higher frequency operation has been shown to increase optical emission output and to enhance the electron density. [35] Extending the operating frequency range may broaden the applicability of the array devices. Another advantage of going to higher frequency is smaller sizes which will then be more feasible in some portable embedded systems.

5.2.2 Increase power level to support larger number of resonators.

Although the circular plasma array is limited in a closed form, the linear array could be expanded to achieve longer plasma lines. The longest array in this work has been shown to be 90 mm long which is moderate in length. There are several challenges when expanding the array. The top concern is what happens when the length of the plasma line becomes comparable to the wavelength at the resonant frequency. It is possible that there would be a standing wave carried by the plasma or on the direct coupling strip which may cause inevitable non-uniformity and even extinguish the microplasma on some of the resonators.

5.2.3 Instability study

First of all, it is common for many atmospheric pressure plasmas to transition into an arc which will damage the circuit and cause the array to be destroyed permanently. So the conditions for arc transition instability will be studied to prevent the array from accidentally operating at those conditions. In addition, the dielectric limiters restrict the area in which plasma can be sustained. Limited plasma may extend both inward and outward with respect to the array. Thus plasma can contact the substrate material which will add more uncertainties to the plasma in terms of uniformity such as flickering and the introduction of contaminants from the substrate.

6 **References**

- [1] U.Kogelschatz, *Fundamentals and applications of dielectric-barrier discharges*, J. PHYS IV FRANCE 7 (1997).
- [2] Se Youn Moon, W. Choe and B. K. Kang, *A uniform glow discharge plasma source at atmospheric pressure*, Applied Physics Letters, Vol. 84, Num 2 2004.
- [3] S. Forster, C. Mohr, W. Viol, *Investigations of an atmospheric pressure plasma jet by optical emission spectroscopy*. Surface and Coatings Technol. Vol.200, Issue 1-4, 2005
- [4] Yong Cheol Hong and Han Sup Uhm, *Microplasma jet at atmospheric pressure*, Applied Physics Letter, Vol. 89, 221504 (2006)
- [5] A. Shashurin, M. N. Shneider, A. Dogariu, R. B. Miles and M. Keidar, *Temporal behavior of cold atmospheric plasma jet*, Applied Physics Letters, Vol. 94, 231504, (2009)
- [6] C.Wang and N. Srivastava, *OH number densities and plasma jet behavior in atmospheric microwave plasma jets operating with different plasma gases(Ar, Ar/N₂, and Ar/O₂)*, Eur. Phys. J. D, 60, 465-478, (2010)
- [7] Jianjun Shi, Fangchun Zhong, and Jing Zhang, D. W. Liu and M. G. Kong, *A hypersonic plasma bullet train traveling in an atmospheric dielectric-barrier discharge jet*, Physics of plasmas, Vol. 15, 013504 (2008)
- [8] B. N. Sismanoglu, K. G. Grigorov, R. A. Santos, R. Caetano, M. V. O. Rezende, Y. D. Hoyer and V. W. Ribas, *Spectroscopic diagnostics and electric field measurements in the near-cathode region of an atmospheric pressure microplasma jet*, Eur. Phys. J. D, 60, 479-487, (2010)
- [9] B. Hrycak, M.Jasinski, and J. Mizeraczyk, *Spectroscopic investigations of microwave microplasmas in various gases at atmospheric pressure*, Eur. Phys. J. D, 60, 609-619 (2010)
- [10] J. L. Walsh and M. G. Kong, *Room-temperature atmospheric argon plasma jet sustained with submicrosecond high-voltage pulses*, Applied Physics Letters, Vol. 91, 221502 (2007)

- [11] J. L. Walsh, J. J. Shi, and M. G. Kong, *Contrasting characteristics of pulsed and sinusoidal cold atmospheric plasma jets*, Applied Physics Letters, Vol. 88, 171501 (2006)
- [12] M. C. Kin, S. H. Yang, J. -H. Boo, J. G. Han, *Surface treatment of metals using an atmospheric pressure plasma jet and their surface characteristics*, Surface and Coatings Technol. 174-175 (2003) 839-844
- [13] S E Babayan, J Y Jeong, A Schutze, V J Tu, Maryam Moravej, G S Selwyn and R F Hicks, *Deposition of silicon dioxide films with a non-equilibrium atmospheric-pressure plasma jet*, Plasma Sources Sci. Technol. 10(2001) 573-578.
- [14] J. F. Kolb, A.-A H. Mohamed, R. O. Price, R. J. Swanson, A. Bowman, R. L. Chiavarini, M. Stacey, and K. H. Schoenbach, *Cold atmospheric pressure air plasma jet for medical applications*, Applied Physics Letters, Vol. 92, 241501 (2008)
- [15] G. S. Selwyn, H. W. Herrmann, J. Park, and I. Henins, *Materials Processing Using an Atmospheric Pressure RF-Generated Plasma Source*, Contrib. Plasma Phys. Vol. (2001) 6, 610-619
- [16] H S Uhm, Y C Hong and D H Shin, *A microwave plasma torch and its applications*, Plasma Sources Sci. Technol. 15 (2006) S26-S34
- [17] R. Dussart, L. J. Overzet, P. Lefauchaux, T. Dufour, M. Kulsreshath, M. A. Mandra, T. Tillocher, O. Aubry, S. Dozias, P. Ranson, J. B. Lee, and M. Goechner, *Integrated microplasma in silicon operating in helium*, Eur. Phys. J. D, 60, 601-608 (2010)
- [18] Z Cao, Q Nie, D L Bayliss, J L Walsh, C S Ren, D Z Wang and M G Kong, *Spatially extended atmospheric plasma arrays*, Plasma Sources Sci. Technol. 19 (2010) 025003
- [19] F. Iza and J. Hopwood, *Low-power microwave plasma source based on a microstrip split-ring resonator*, IEEE Trans. Plasma Sci. 31 782 (2003)
- [20] David M. Pozar, *Microwave engineering*, 3rd Edition, John Wiley & Sons, 2004
- [21] F. Iza and J. Hopwood, *Split-ring resonator microplasma: microwave model*,

plasma impedance and power efficiency, Plasma Sources Sci. and Technol. 14 (2005) 397-406

[22] Z.-B. Zhang, J. Hopwood, *Linear arrays of stable atmospheric pressure microplasmas*, Appl. Phys. Lett. 95, 16502 (2009)

[23] H.A. Haus, W. Huang, *Coupled-Mode Theory*, Proc. IEEE 79,1505(1991)

[24] C. Wu, Z.-B Zhang, A. Hoskinson, J. Hopwood, *Circular array of stable atmospheric pressure microplasmas*, Eur. Phys. J. D, 60, 621-625(2010)

[25] ZhiBo Zhang, *Linear Arrays of Stable Atmospheric Pressure Microplasma*, Master Thesis, Tufts University, 2010

[26] Yo-Shen Lin and Chun Hsiung Chen, *Novel Balanced Microstrip Coupled-line Bandpass Filters*, URSI EMTS 2004

[27] Jia-Sheng Hong, Michael J. Lancaster, *Design of Highly Selective Microstrip Bandpass Filters with a Single Pair of Attenuation Poles at Finite Frequencies*, IEEE Trans., vol. 48, No. 7, 2000

[28] Eunyoung Park and Chulhun Seo, *Low Phase Noise Oscillator Using Microstrip Square Open Loop Resonator*, IEEE MTT-s International, Microwave Symposium Digest, 2006

[29] Chu-Yu Chen and Cheng-Ying Hsu, *A Simple and Effective Method for Microstrip Dual-Band Filters Design*, IEEE Microwave and wireless components letters, vol. 16, No. 5, 2006

[30] Jia-Sheng Hong, Micheal J. Lancaster, *Theory and Experiment of Novel Microstrip Slow-Wave Open-Loop Resonator Filters*, IEEE Trans., vol. 45, No.12 1997

[31] Jen-Tsai Kuo, Meshon Jiang and Hsien-Jen Chang, *Design of Parallel-Coupled Microstrip Filters With Suppression of Spurious Resonances Using Substrate Suspension*, IEEE Trans., vol. 52, No.1 2004

[32] Sang-June park, Koen Van, Gabriel M. Rebeiz, *A Miniature 2.1-GHz Low Loss Microstrip Filter With Independent Electric and Magnetic Coupling*, IEEE Microwave and wireless components letters, vol. 14, No. 10, 2004

[33] J.-S. Hong, *Couplings of asynchronously tuned coupled microwave resonators*.

IEEE Proc. Microw. Antennas Propag., Vol. 147, No. 5, October 2000

[34] Ikuo Awai and Yangjun Zhang, *Coupling Coefficient of Resonators-An Intuitive Way of Its Understanding*, Electronics and Communications in Japan, Part 2, vol. 90, No. 9, 2007

[35] Jun Xue, Jeffrey Hopwood, *Microwave-frequency effects on microplasma*, IEEE Trans. On plasma science, vol.37, No. 6, 2009

Appendix A: MATLAB code for CMT model of 72-resonator linear array

```

clear;clc;
%Resonant frequency (in MHz)
wo=465;
%Damping (in MHz)
L=1;
%First order coupling (in MHz)
k1=-40; %this coupling frequency comes the freq-splitting simulation of two
        %resonators, separated by 1 mm, using Ensemble
        %seems to match experiments only if the coupling is negative (180d)
        % general mxm with 5th order coupling
m=72;
k2=-31;
k3=-18;
k4=-9;
%k5=k1*0.1;
w=450;
    d=ones(m,1)*wo-w+j*L;
    f=ones(m-1,1)*k1;
    g=ones(m-2,1)*k2;
    h=ones(m-3,1)*k3;
    p=ones(m-4,1)*k4;
    %q=ones(m-5,1)*k5;% Ignore effect from the lines that are far away from
    %the one .

M=diag(d,0)+diag(f,1)+diag(f,-1)+diag(g,2)+diag(g,-2)+diag(h,3)+diag(h,-3)+diag(p,4)+diag(p,-4);
    % +diag(q,5)+diag(q,-5);
x=zeros(m,m);x(1,1)=-50;%x(2,2)=-0;%resonant frequency shift at resonator
one.
    %M=M+x;
[V,D]=eig(M);
eig(M)+w;
figure
hold on
%plot(abs(V(:,1))+0.5*(V(:,2))+0.25*(V(:,3))), 'o')
%add the three freq
plot(abs(V(:,1)),'blue-+')
%plot(abs(V(:,2)),'black-')
%plot(abs(V(:,3)),'g-')
%plot(abs(V(:,4)),'p')
% plot((abs(V(:,1))+0.5*abs(V(:,2))+0.25*abs(V(:,3))), 'r-o')
    %multiplexing the three frequencies
% Rt1=0.89;

```

```
% Rt2=0.11;  
%Rt3=0.03;  
%plot((Rt1*abs(V(:,1))+Rt2*abs(V(:,2))), 'r-o')  
grid on;  
%legend('1st mode', '2nd mode', 'Superposition of the first two modes')  
xlabel('Resonator Number')  
ylabel('Energy Ratio')
```

Appendix B: MATLAB code for CMT model of 72-resonator array with DCS

[illegible]

```

xlim([1 m]);
%plot(abs(V(:,2)), 'black-.' )
%plot(abs(V(:,3)), 'g-.' )
%plot(abs(V(:,4)), 'p')
%plot((abs(V(:,1))+0.5*abs(V(:,2)))+0.25*abs(V(:,3))),
'r-o') %multiplexing the three frequencies
Rt1=0;
Rt2=1;
%Rt3=0.03;
plot((Rt1*abs(V(:,1))+Rt2*abs(B)'), 'r-o')
grid on;
%legend('1st mode', '2nd mode', 'Superposition of the first two modes')
xlabel('Resonator Number')
ylabel('Energy Ratio')

```

Appendix C: MATLAB code for CMT model of circular array without plasma effect

```

clear;clc;
%Resonant frequency (in MHz)
wo=1000;
%Damping (in MHz)
L=1;
%First order coupling (in MHz)
k12=-26; %this coupling frequency comes the freq-splitting simulation of
two resonators, separated by 1 mm, using Ensemble
% seems to match experiments only if the coupling is negative (180d)
% general mxm with 5th order coupling
m=6;
k13=-5;
k14=-5;
w=1000;
d=ones(m,1)*wo-w+j*L;
f=ones(m-1,1)*k12;
g=ones(m-2,1)*k13;
h=ones(m-3,1)*k14;
p=ones(m-4,1)*k13;
q=ones(m-5,1)*k12;% only consider the coupling coefficients of the
neighboring 3 lines Ignore effect from the lines that are far away from the one .

M=diag(d,0)+diag(f,1)+diag(f,-1)+diag(g,2)+diag(g,-2)+diag(h,3)+diag(
h,-3)+diag(p,4)+diag(p,-4)+diag(q,5)+diag(q,-5);
%c=zeros(m,1);c(1,1)=-20;N=diag(c);M=M+N;
[V,D]=eig(M);
eig(M)+w;
figure
hold on
%plot(abs(V(:,1))+0.5*(V(:,2))+0.25*(V(:,3))), 'o') %add the three freq
plot(abs(diag(V(:,1)*transpose(V(:,1)))),'blue o','MarkerSize',14);
plot(abs(diag(V(:,2)*transpose(V(:,2)))),'black *','MarkerSize',14);
plot(abs(diag(V(:,3)*transpose(V(:,3)))),'g^','MarkerSize',14);
plot(abs(diag(V(:,4)*transpose(V(:,4)))),'rx','MarkerSize',14);
legend('mode 1','mode 2','mode 3','mode 4');
xlabel('Resonator Number');ylabel('|a_m|^2');
%plot(abs(V(:,5)), 'k-')
%plot(abs(V(:,6)), 'b')
%grid on

```

Appendix D: MATLAB code for CMT model of circular array with plasma effect

```

clear;clc;
%Resonant frequency (in MHz)
wo=1000;
%Damping (in MHz)
L=1;
%First order coupling (in MHz)
k12=-26; %this coupling frequency comes the freq-splitting simulation of
two resonators, separated by 1 mm, using Ensemble
% seems to match experiments only if the coupling is negative (180d)
% general mxm with 5th order coupling
m=6;
k13=-5;
k14=-5;
w=1000;
d=ones(m,1)*wo-w+j*L;
f=ones(m-1,1)*k12;
g=ones(m-2,1)*k13;
h=ones(m-3,1)*k14;
p=ones(m-4,1)*k13;
q=ones(m-5,1)*k12;% %only consider the coupling coefficients of the
neighboring 3 lines Ignore effect from the lines that are far away from the one .

M=diag(d,0)+diag(f,1)+diag(f,-1)+diag(g,2)+diag(g,-2)+diag(h,3)+diag(
h,-3)+diag(p,4)+diag(p,-4)+diag(q,5)+diag(q,-5);
c=zeros(m,1);c(1,1)=-20;N=diag(c);M=M+N;
[V,D]=eig(M);
eig(M)+w;
figure
hold on
%plot(abs(V(:,1))+0.5*(V(:,2))+0.25*(V(:,3))), 'o') %add the three freq
plot(abs(diag(V(:,1)*transpose(V(:,1)))),'blue o','MarkerSize',14);
plot(abs(diag(V(:,2)*transpose(V(:,2)))),'black *','MarkerSize',14);
plot(abs(diag(V(:,3)*transpose(V(:,3)))),'g^','MarkerSize',14);
plot(abs(diag(V(:,4)*transpose(V(:,4)))),'rx','MarkerSize',14);
legend('mode 1','mode 2','mode 3','mode 4');
xlabel('Resonator Number');ylabel('|a_m|^2');
%plot((abs(V(:,1))+0.5*abs((V(:,2))+0.25*abs(V(:,3))),
'r-o') %multiplexing the three frequencies
%plot((Rt1*abs(V(:,1))+Rt2*abs(V(:,2))), 'r-o')
%legend('1st mode', '2nd mode', 'Superposition of the first two modes')
%xlabel('Resonator Number')
%ylabel('Energy Ratio')

```